# UC San Diego

## UC San Diego Electronic Theses and Dissertations

**Title**

Patient-specific modeling of cardiac electromechanics in dyssynchronous heart failure

**Permalink**

https://escholarship.org/uc/item/4r99j9th

**Author**

Shin, Jun Seob

**Publication Date**

2009

Peer reviewed|Thesis/dissertation

eScholarship.org Powered by the California Digital Library
University of California

UNIVERSITY OF CALIFORNIA, SAN DIEGO

# Patient-specific Modeling of Cardiac Electromechanics in Dyssynchronous Heart Failure

A Thesis submitted in partial satisfaction of the requirements
for the degree Master of Science

in

Bioengineering

by

Jun Seob Shin

Committee in Charge:

Professor Andrew D. McCulloch, Chair
Professor Jeff Omens
Professor John Watson

2009

The Thesis of Jun Seob Shin is approved, and it is acceptable

in quality and form for publication on microfilm and electronically:

_____

_____

_____
Chair

University of California, San Diego

2009

*To my parents for their unconditional love*

# TABLE OF CONTENTS


Signature page . . . . . iii

Dedication . . . . . iv

Table of Contents . . . . . v

List of Figures . . . . . vii

List of Tables . . . . . x

Acknowledgments . . . . . xi

Abstract . . . . . xiii

Chapter 1: Background . . . . . 1
1.1 Cardiac Physiology . . . . . 1
1.1.1 Cardiac Anatomy . . . . . 1
1.1.2 Fiber Architecture . . . . . 3
1.1.3 Cardiac Electrophysiology . . . . . 7
1.2 Cardiac Mechanics . . . . . 11
1.2.1 Global Ventricular Function . . . . . 11
1.2.2 Myocardial Passive Mechanical Properties . . . . . 13
1.2.3 Myocardial Active Mechanical Properties . . . . . 15
1.3 Congestive Heart Failure . . . . . 16
1.4 Cardiac Resynchronization Therapy . . . . . 19
1.5 Computational Modeling . . . . . 21
1.6 Goals . . . . . 22

Chapter 2: Materials and Methods . . . . . 25
2.1 Patient Recruitment and Bi-ventricular ICD Implantation . . . . . 25
2.2 Clinical Measurements . . . . . 26
2.2.1 Cardiac Computed Tomography . . . . . 26
2.2.2 ECG and Left Ventricular Pressure Recordings . . . . . 27
2.2.3 Electroanatomic Mapping of Activation Times . . . . . 27
2.2.4 Transthoracic Echocardiography . . . . . 28
2.2.5 Diffusion Tensor Magnetic Resonance Imaging . . . . 29
2.3 Data Processing and Model Development .. . . . . 30
2.3.1 Modeling Three-dimensional Ventricular Geometry . . 30

2.3.1.1 Image Segmentation . . . . . 30
2.3.1.2 Singular Value Decomposition . . . . . 33
2.3.1.3 Two-dimensional Mesh Fitting . . . . . 36
2.3.1.4 Three-dimensional Mesh Generation . . . . . 41
2.3.2 Modeling Fiber Architecture . . . . . 41
2.3.2.1 DTMRI Background . . . . . 41
2.3.2.2 DTMRI Processing . . . . . 44
2.3.2.3 Fiber Mapping . . . . . 48
2.3.3 Endocardial Activation Time Fitting . . . . . 50
2.3.4 Estimation of Left Ventricular Cavity Volumes . . . . . 53

Chapter 3: Results . . . . . 54
3.1 Cardiac Computed Tomography and Image Segmentation . . . . . 54
3.2 Singular Value Decomposition and Geometric Model Development . . . . . 56
3.3 DTMRI Processing and Fiber Mapping . . . . . 60
3.4 Endocardial Activation Time Mapping . . . . . 65
3.6 Dynamic Ventricular Volumes and Pressures . . . . . 69

Chapter 4: Discussion . . . . . 72
4.1 Cardiac CT and Image Segmentation . . . . . 73
4.2 DTMRI and Fiber Architecture . . . . . 76
4.3 Endocardial Activation Maps . . . . . 77
4.4 LV Volume Estimation . . . . . 79

Chapter 5: Conclusions . . . . . 81

References . . . . . 86

# LIST OF FIGURES


Figure 1.1: Longitudinal cross-section of the heart . . . . . 2

Figure 1.2: A schematic depicting the myofibers and the laminar structure of the myocardial tissues . . . . . 4

Figure 1.3: Schematic illustration of a transmural block of myocardium . . . . 5

Figure 1.4: Typical measurement of fiber angles in successive sections from a heart and fiber angles estimated using Diffusion Tensor Magnetic Resonance Imaging . . . . . 5

Figure 1.5: Different action potential shapes of cardiac cells . . . . . 9

Figure 1.6: Schematic diagram of left ventricular pressure-volume loops . . 13

Figure 1.7: Workflow for design of patient-specific model to predict the outcome of CRT . . . . . 24

Figure 2.1: Overview of the Manual Segmentation process using ITK-SNAP and MATLAB . . . . . 31

Figure 2.2: The geometrical meaning of SVD . . . . . 35

Figure 2.3: Transformation from CT image coordinate system to reference coordinate system in Continuity . . . . . 35

Figure 2.4: An ellipsoidal mesh in prolate spheroidal coordinate system ($\Lambda$, M, $\Theta$) and its relationship to rectangular Cartesian coordinate system ($Y_1$, $Y_2$, $Y_3$) . . . . . 37

Figure 2.5: The initial finite element surface model used for fitting. . . . . 39

Figure 2.6: Top (left) and Anterior (right) views of the initial mesh with data points . . . . . 39

Figure 2.7: Images showing the x, y, and z components of the primary eigenvector for slice 50 of a normal human heart . . . . . 45

Figure 2.8: Images showing the 6 Independent components of the diffusion tensor *D* for slice 50 of a normal human heart . . . . . 46

Figure 2.9: Geometric 3D finite element model of the normal human heart . . . . . 49

Figure 2.10: A cubic element and synthetic data used to test the fiber mapping method . . . . . 50

Figure 2.11: Activation time data points rendered on LV and RV endocardial surfaces . . . . . 52

Figure 3.1: Contiguous axial CT slices of voxel thickness 1.25mm . . . . . 55

Figure 3.2: Endocardial and epicardial boundary contours manually delineated from the axial CT slices . . . . . 55

Figure 3.3: Comparison between the LV boundary data points in their original configuration and after transformations have been applied . . . . . 57

Figure 3.4: Boundary data points of all anatomic structures after transformations have been performed . . . . . 57

Figure 3.5: Effect of the smoothing weight, α on the RMS fitting error . . . . 58

Figure 3.6: Top view of the 2D mesh fitted to the data points . . . . . 59

Figure 3.7: Posterior view of the 2D finite element surface model . . . . . 59

Figure 3.8: 3D finite element model of the failing heart . . . . . 60

Figure 3.9: Fiber mapping results with trilinear basis functions on a single cubic element . . . . . 61

Figure 3.10: Fiber mapping results with trilinear basis functions on a two-element cubic mesh . . . . . 62

Figure 3.11: Comparison between fiber angles from synthetic data and those computed from eigenvectors as a result of eigenvalue decomposition at Gauss points . . . . . 63

Figure 3.12: 3D finite element model of the normal human heart from JHU DTMRI data, showing the fiber orientation with primary eigenvectors throughout the myocardium . . . . . 65

Figure 3.13: Isochronal maps of LV and RV activation times generated by Ensite NavX system . . . . . 66

Figure 3.14: Activation time data points projected and fitted on the LVendocardial surface . . . . . 67

Figure 3.15: Activation time data points projected and fitted on the RV endocardial surface . . . . . 67

Figure 3.16: Effect of smoothing weight on RMS fitting errors for LV and RV endocardial activation time fitting . . . . . 68

Figure 3.17: Endocardial activation time map transferred from 2D to 3D finite element model . . . . . 68

Figure 3.18: Four-chamber and two-chamber views of 2D transthoracic Echocardiograms obtained at end-diastole and at end-systole with Bi-VICD turned on . . . . . 70

Figure 3.19: ECG and LV pressures measured using Clearsign$^{TM}$ Bard electrophysiologic recorder system with Bi-V ICD turned off . . . 71

Figure 4.1: CT images showing artifacts. . . . . 74

Figure 4.2: Results of a semi-automatic segmentation using active contour methods . . . . . 76

# LIST OF TABLES


Table 1.1: NYHA Functional Classification of heart failure . . . . . 17

Table 3.1: RMS fitting errors for diffusion coefficients using different basis functions and number of elements . . . . . 61

Table 3.2: RMS errors and maximum absolute differences between fiber angles from synthetic data and those computed from different combinations of basis functions and number of elements for fitting diffusion coefficients. . . . . 63

Table 3.3: RMS fitting errors for diffusion coefficients and their ranges . . . 64

Table 3.4: Local Activation Time measurements in LV and RV . . . . . 65

Table 3.5: Comparison between LV volumes from cardiac echo reports and those calculated using Simpson's method . . . . . 71

# ACKNOWLEDGMENTS

I would like to express my appreciation to my family, colleagues and professors without whose support and encouragement this work would not have been possible. First and foremost, I would like to thank my advisor, Dr. Andrew McCulloch, for giving me the opportunity to conduct research in the fascinating field of cardiac mechanics. I am very grateful for his professional guidance and amazed by his scientific insights and knowledge. I would also like to thank Dr. Roy Kerckhoffs, for his enormous patience, encouragement and willingness to help when I am struggling and frustrated. I cannot imagine what it would have been like without his invaluable experience and day-to-day help that answered millions of my questions. I would also like to express my thankfulness to Dr. David Krummen for his constant encouragements, patience, and many helpful discussions and Dr. Paul Stark, for willingly providing his expertise to help my project move forward.

I would like to give special thanks to everyone in the lab who gave me suggestions and helped me on my project, especially Fred Lionetti and Ankur Jain, who spent a lot of time trying to help me with Python programming, debugging, and answering my questions regarding technical aspects of Continuity 6.3.

I would also like to take this opportunity to thank my colleagues in the Department of Bioengineering. Namgyun Lee, who would spend more time

helping me with useful discussions and advice than his own work even during his busiest times. Saleh Amirriazi, for his consistent support, friendship, help and all the memories throughout the master's program as well as the undergraduate program at UCSD. Katie Olson, Veronica Neiman, and Jayant Menon, for their friendship, encouragements, discussions, and most importantly, for being part of the team Tritonics to pursue exceptionally remarkable things that would not be possible if it wasn't as a team. I am very privileged to have met them and very proud of all our efforts to turn our passion into something that will change the world.

Lastly, I would like to express my deepest gratitude to my parents in Korea for their unremitting, unwavering, and unconditional love, consolation and support throughout the past 6 years since I came to the United States. I am very grateful for their constant faith in me and always encouraging me to pursue my dreams throughout my life. It is to them that I dedicate this work.

**ABSTRACT OF THE THESIS**

Patient-specific Modeling of Cardiac Electromechanics in Dyssynchronous Heart Failure

by

Jun Seob Shin

Master of Science in Bioengineering

University of California, San Diego, 2009

Professor Andrew McCulloch, Chair

Cardiac resynchronization therapy (CRT) is an increasingly popular therapy for heart failure patients with intraventricular conduction delay, such as left bundle branch block. However, clinical trials with CRT have revealed that about 30% of patients may be classified as non-responders mainly due to a lack of predictive, mechanism-based objective criteria for patient selection. In addition,

even responders exhibit variable degrees of benefit from the therapy, implying that it is not always performed in an optimal fashion. In order to predict and optimize the outcomes of CRT on individual patients, methods for generating anatomically detailed three-dimensional finite element models of failing human heart and estimating various patient-specific model parameter values from clinical measurements in heart failure patients are developed. The three-dimensional finite element model was generated from cardiac computed tomography images obtained at end-diastole. The fiber architecture was modeled by computing the eigenvectors from nodal fields of diffusion coefficients obtained from diffusion tensor magnetic resonance imaging (DTMRI). The endocardial activation maps, which serve as initial conditions in estimating the three-dimensional activation sequence of the myocardium, were generated by fitting endocardial activation time measurements from electroanatomic mapping. Lastly, a method for estimating left ventricular volumes from transthoracic echocardiograms was proposed. These methods provide efficient techniques to estimate patient-specific model parameters and therefore, will prove useful in patient-specific model development and ultimately, in predicting clinical outcomes of CRT on individual heart failure patients.

# Chapter 1

# Background

## 1.1 Cardiac Physiology

### *1.1.1 Cardiac Anatomy*

The heart is a muscular organ whose primary function is to pump oxygen-rich blood and various nutrients to all living cells in the body. This is achieved through its four chambers: the left and right atria and the left and right ventricles. The right atrium (RA) receives the oxygen-deprived blood from the systemic circulation and fills the right ventricle (RV), which then pumps the blood to the lungs where it becomes oxygen-enriched again through gaseous exchange. The oxygenated blood then returns to the left atrium (LA) through pulmonary veins

and flows into the left ventricle (LV), where it is ejected through the aorta to the rest of the body. A schematic of the detailed anatomy of the heart is shown in Figure 1.1.

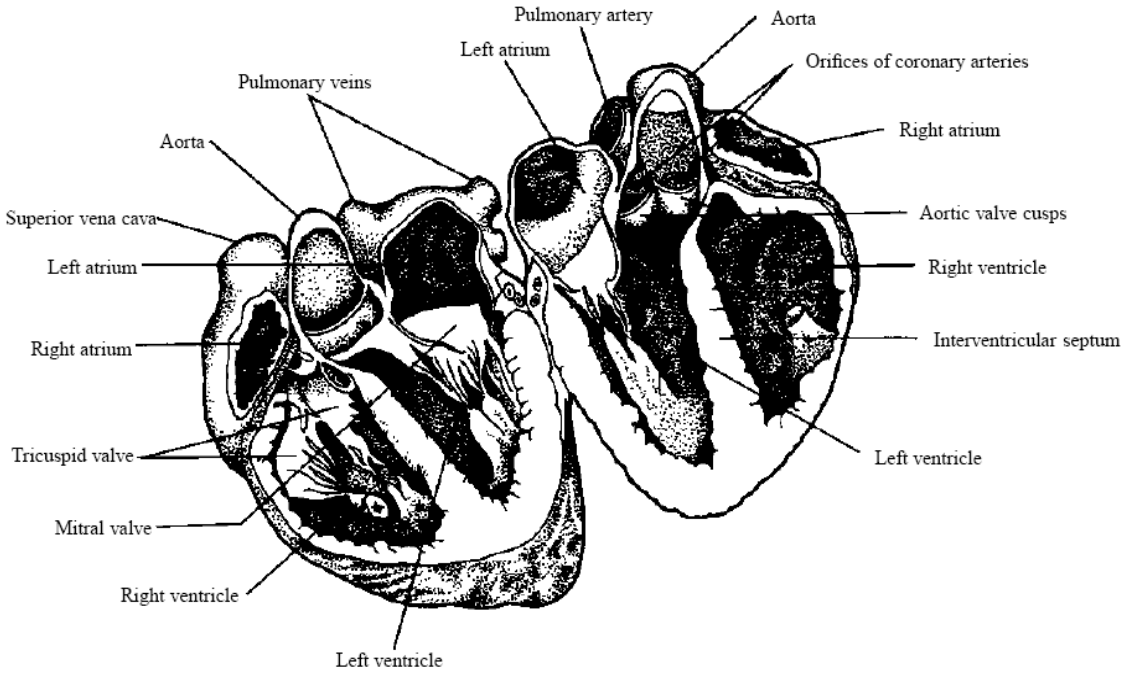


**Figure 1.1:** Longitudinal cross-section of the heart. Source: Katz 2001 [1]

The heart valves are the main structures that help maintain unidirectional flow of blood within the heart by opening and closing depending on the pressure difference across them. The *atrioventricular* (AV) valves are located between the atria and the ventricles and are anchored to the ventricular wall by *chordate tendineae*, which are connected to the *papillary muscles* that limit their movements and thus, prevent their inversion. When the blood pressure in an atrium exceeds that in the ventricle, the valve is opened to permit blood flow from

atrium to ventricle. On the other hand, when the pressure inside a ventricle exceeds that in the atrium due to ventricular contraction, the AV valve between them closes and allows blood to flow only into the pulmonary trunk from the right ventricle and into the aorta from the left ventricle, but not back into the atrium. The AV valve between the RA and the RV is named the *tricuspid valve* as it consists of 3 flaps as opposed to the *bicuspid* (or *mitral*) *valve* located between the LA and the LV. The *semilunar valves*, on the other hand, are located between the outflow tracts of the ventricles and the great arteries into which each ventricle ejects blood: the pulmonary artery and the aorta. Thus, they are termed the *pulmonic* and *aortic valves*. They act in a purely passive fashion like the AV valves to permit flow of blood into the arteries during ventricular contraction, but prevent the backward movement of blood during ventricular relaxation.

### *1.1.2 Fiber Architecture*

The cardiac ventricular tissue exhibits a highly complex three-dimensional (3D) muscle fiber architecture [2], which has an effect on the electrical and mechanical functions of the heart. In order to understand how the microstructure of the heart affects its electrical and mechanical functions, it is important to quantitatively describe the cellular architecture and the connective tissue associated with the ventricles. Detailed evaluations of the microstructural architecture of the myocardial tissue have revealed that the cardiac tissue is a composite of discrete layers of myocardial muscle fibers organized into a complex arrangement called laminae or sheets consisting of 3 to 4 layers of

myofibers (Figure 1.2) [3]. The myocardial sheets are connected to each other by the loose connective tissue. Such a well-defined hierarchical structure of the fibers and sheets allows the myocardial muscles to work in a mechanically optimal manner to pump blood efficiently to various parts of the body. Several investigators have utilized both experimental measurements and computational models of cardiac mechanics to show that such a microsctrctural organization of myofibers contributes to uniform distribution of stress and strain along the fiber direction during a cardiac cycle [4].

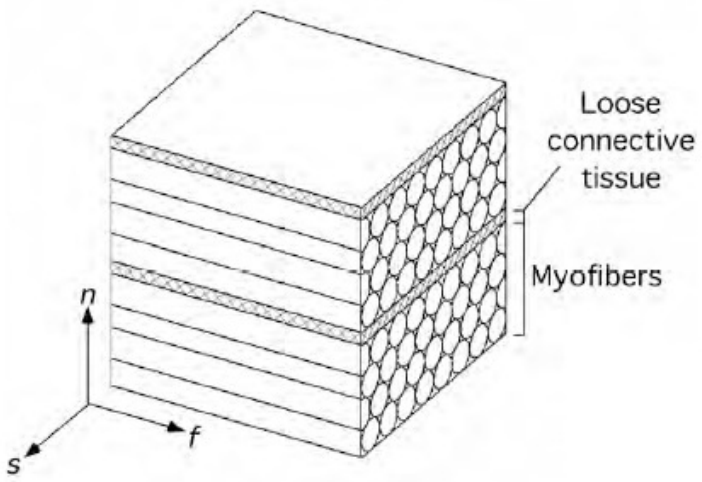


**Figure 1.2**: A schematic depicting the myofibers and the laminar structure of the myocardial tissues. Source: Ennis DB 2004 [5]

Gross dissections and histological measurements of selected tissue regions have revealed that myocytes are helically wound around the chambers and that there is a transmural variation of fiber orientations (Figure 1.3) [6-9]. The fiber angles, which are measured from the horizontal plane, increase almost linearly as a function of transmural depth from -60$^{o}$ at the epicardium, to 0$^{o}$ at the

mid-wall and eventually, to +60$^{o}$ at the endocardium (Figure 1.4). However, the orientation of myocardial sheets is different throughout the ventricular wall.

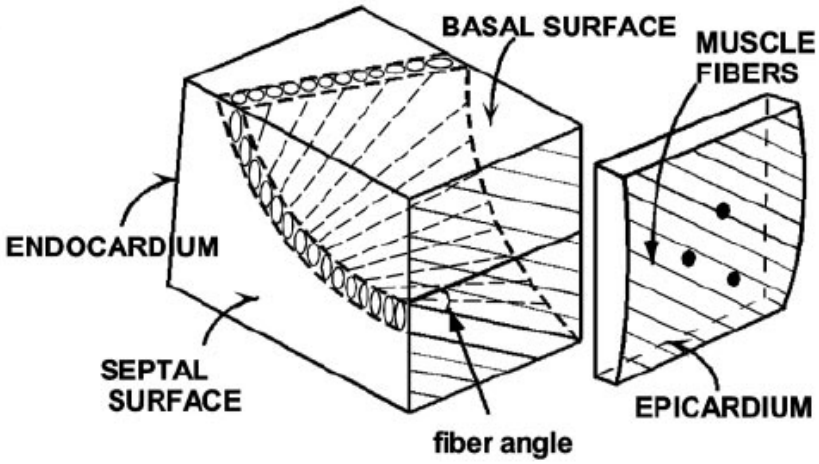


**Figure 1.3:** Schematic illustration of a transmural block of myocardium. Source: Takayama 2002 [10]

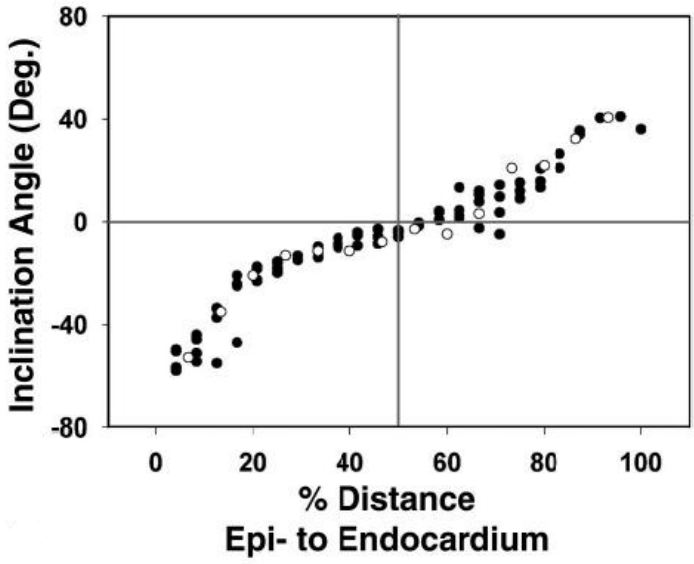


**Figure 1.4:** Typical measurement of fiber angles in successive sections from a heart (open circles) and fiber angles estimated using Diffusion Tensor Magnetic Resonance Imaging (closed circles). Source: Scollan *et al* [11]

The effects of fiber architecture on the mechanics of the ventricular myocardium have been investigated [10, 12-15]. These studies have demonstrated that a detailed knowledge of the ventricular fiber structure is crucial in understanding of cardiac function in both healthy and diseased hearts as it has a significant influence on their electromechanics.

Although fiber architecture varies from patient to patient, information about fiber architecture cannot be obtained patient-specifically with currently available technologies, such as histology and Diffusion Tensor Magnetic Resonance Imaging (DTMRI). Histological methods require sacrificing an animal to explant the heart for fiber angle measurements, and the procedure usually takes several months to acquire a complete set of measurements for a single heart. Another limitation of this method is the low spatial resolution (~0.5 × 0.5 × 2mm). Recent advancements in DTMRI have made it possible to overcome some of the limitations of histological methods by providing a way to acquire high resolution images (350 μm in-plane and 800 μm out of plane) that contain information about fiber orientations in a significantly reduced period of time (~20hrs). However, DTMRI also requires that the heart is explanted and therefore, this technique is, at least currently, not feasible to be used clinically. Fortunately, studies have shown that fiber architecture is conserved across individuals in species at least when geometric variations are accounted for [16]. Therefore, it is reasonable to assume that the fiber orientations from a DTMRI data set for a heart that belongs to an individual are representative of those of another. This allows for

construction of patient-specific computational models that incorporate detailed information about the fiber architecture of the human heart.

### *1.1.3 Cardiac Electrophysiology*

In order to achieve efficient pumping of blood, the heart possesses a specially designed conduction system responsible for both generating electrical impulses that cause rhythmical contractions of the cardiac muscle and rapidly conducting the impulses throughout the heart. Cardiac muscle, when triggered by depolarization of the plasma membrane, undergoes contraction as the gap junctions between cardiac myocytes allow action potentials to propagate from one cell to another. Therefore, the initial depolarization that occurs in the *sinoatrial* (SA) node in the right atrium is able to spread throughout the atria and the ventricles. The action potential initiated in the SA node, which acts as the "natural pacemaker" of the heart, first spread rapidly through the cardiac myocytes of the two atria, causing them to contract at nearly the same time. Then, the action potential causes depolarization of the *atrioventricular* (AV) node, which is located at the base of the right atrium and acts as a link between atrial depolarization and ventricular depolarization. One of the most important functions of the AV node is to delay the action potential propagation from the atria to the ventricles to allow sufficient time for the atria to eject blood out into the ventricles before ventricular contraction is initiated. Once the electrical impulse has passed the AV node, it enters the interventricular septum where the conduction system fibers, known as the *bundle of His*, separate into right and left bundle branches,

which enter the wall of both ventricles and make contact with *Purkinje fibers* that allow rapid conduction of impulses throughout the ventricles. Interestingly, the conduction systems of the atria and the ventricles are completely separated from each other by a layer of non-conducting connective tissue, and the AV node and the *bundle of His* together act as the only electrical link between them, ensuring that depolarization of cardiac myocytes occur in the right sequence to achieve efficient pumping of blood. Moreover, the diffuse distribution of the *Purkinje fibers* and their ability to rapidly conduct electrical impulses cause simultaneous depolarization of all ventricular myocytes and thus, ensure a single coordinated contraction of the heart.

Different kinds of cardiac cells produce different shapes of action potentials as they express unique sets of ion channels as shown in Figure 1.5. Particularly, Figure 1.5A shows a typical membrane potential recording from a ventricular muscle cell with five distinct phases that are mainly due to the time-dependent changes of plasma membrane permeabilities for the three major ions, $Na^+$, $Ca^{2+}$, and $K^+$. The presence of a leaky $K^+$ channel keeps the resting membrane potential at a value close to the $K^+$ equilibrium potential(-90 mV) (Phase 4). When a stimulus, such as a wave of depolarization originating from the SA nodal cells, is applied to the ventricular muscle cell, the membrane potential rises and eventually, reaches the threshold voltage. Such a change in the membrane potential causes opening of voltage-gated $Na^+$ channels, and thus, increases their membrane permeabilities. This leads to a sudden influx of $Na^+$

ions, which causes depolarization of the cell (Phase 0). This is followed by a brief partial repolarization due to the efflux of $K^+$ through the transient outward current (Phase 1). The membrane potential then reaches a plateau of about 0 mV as the $K^+$ permeability is kept below the resting value while the $Ca^{2+}$ membrane permeability increases greatly (Phase 2). Therefore, the net influx of $Ca^{2+}$ ions is balanced by the efflux of $K^+$ ions. Finally, repolarization of the cell takes place when the $Ca^{2+}$ channels undergo inactivation and net efflux of $K^+$ ions occurs (Phase 3).

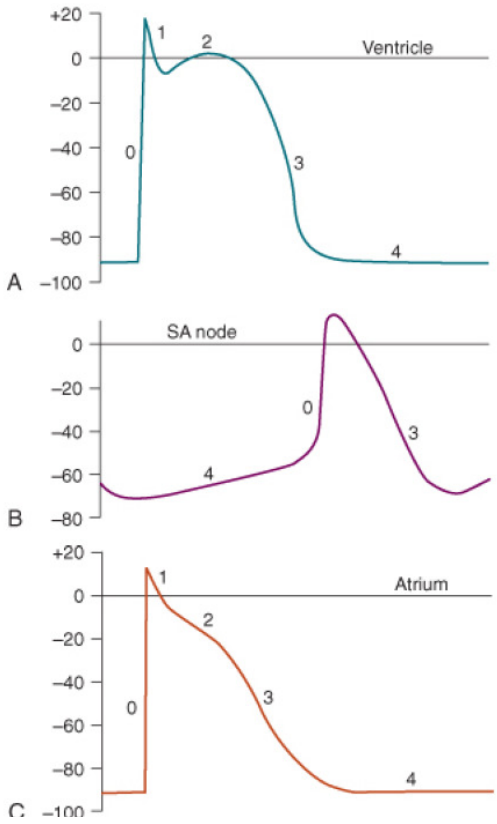


**Figure 1.5:** Different action potential shapes of cardiac cells in the A) ventricle, B) SA node, C) Atrium. Source: Levy *et al* 2006 [17]

In a normal, healthy heart, the electrical impulses generated from the SA nodal cells propagate in such a way that depolarization of ventricular muscle cells always occurs from the endocardium to the epicardium. In addition, depolarization and contraction of ventricular muscle cells spread from the apex toward the base of the ventricles, producing an upward squeezing motion from the bottom for efficient pumping of blood. Therefore, an optimal cardiac function requires a proper, synchronous sequence of activation. However, the activation sequence of myocardium is inhomogeneous and may vary between individuals. To make the matter worse, the activation sequence is often altered in patients with dyssynchronous heart failure, especially when conduction defects, such as left bundle branch block (LBBB), are involved. Thus, synchrony of regional myocardial contraction is disturbed, leading to impairment of the ventricular systolic function. Such characteristics of the conduction system of the heart make it difficult to model structurally. Instead, the patient-specific effects of conduction defects are modeled by prescribing endocardial activation times as initial conditions and varying parameters such as monodomain conductivities and endocardial stimuli to match the mapped and predicted endocardial activation patterns. With best-estimate monodomain conductivities, it is possible to calculate electrical activation times throughout the whole myocardium.

## 1.2 Cardiac Mechanics

The heart is a highly complex organ whose geometry, structure and boundary conditions are often irregular and three-dimensional, heterogeneous and time-varying. In addition, the constitutive properties of the myocardium are nonlinear, anisotropic, and heterogeneous. These structural properties are important parameters that determine the mechanical pump function of the heart. Enormous efforts have been dedicated, over past several decades, to formulate and validate mathematical descriptions, called the constitutive laws, of such complex natures of the ventricular myocardium for passive and active global and regional mechanics. In this section, an overview of global ventricular function is presented, followed by brief descriptions of passive and active mechanical properties of the myocardium relevant to this project.

### *1.2.1 Global Ventricular Function*

The heart is a muscular organ that cyclically generates pressure to pump blood throughout the body's circulation system. The cyclic mechanical function of the heart can be illustrated using the left ventricular pressure-volume relation, a state-space representation of cardiac function in which the left ventricular pressure at each instant during the cardiac cycle is described as a function of the volume at the same instant (Figure 1.6). The cardiac cycle is divided into two major cardiac phases: systole and diastole, which can be further separated into ventricular filling, isovolumic contraction, ejection, and isovolumic relaxation.

These separations are generally defined by the opening and closure of *aortic* and *mitral valves*. Systole begins as the ventricle undergoes isovolumic contraction immediately after the closure of the *mitral valve* (MVC). During isovolumic contraction, the LV pressure increases while the LV volume remains constant. As soon as the LV pressure exceeds the aortic diastolic pressure, the *aortic valve* opens (AVO) and ejection of blood occurs. During the ejection phase, the LV volume decreases while LV pressure first increases to its peak value, known as peak systolic pressure, and then decreases as the ventricle relaxes. The beginning of diastole is marked by the closure of the *aortic valve* (AVC), which stops ejection of blood and the ventricle undergoes isovolumic relaxtion, in which the LV pressure decreases with constant LV volume. When the LV pressure falls below the left atrial pressure, the *mitral valve* opens (MVO) and ventricular filling occurs.

Whenever there is an increase in the afterload, there is a predictable amount of increase in the volume ejected by the left ventricle and thus, connecting the points at corresponding times in different cardiac cycles results in a linear relationship with a nearly constant intercept on the volume axis, representing the end-systolic LV volume. The end-systolic pressure volume relation (ESPVR) is an example of such lines which occurs at end-systole. The slope of ESPVR serves as an index of cardiac contractility. It is sensitive to functional impairment in disorders such as ischemic heart disease, and is often used clinically in quantifying ventricular pumping function. The end-diastolic pressure-volume relation (EDPVR) can be obtained in a similar manner. The

EDPVR is determined mainly by geometric parameters including chamber dimension and wall thickness, the material properties of diastolic myocardium, and boundary conditions.

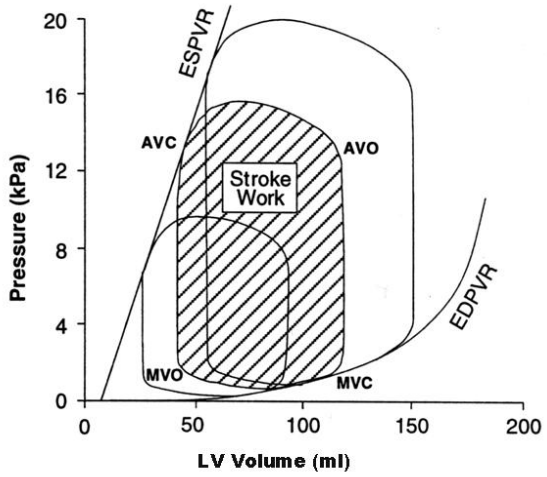


**Figure 1.6:** Schematic diagram of left ventricular pressure-volume loops. The end-systolic pressure-volume relation (ESPVR) and the end-diastolic pressure volume relation (EDPVR) are shown also shown. The area within the loop represents the external stroke work for a single heart beat. The effects of changing end-diastolic pressure (preload) and end-systolic pressure (afterload) are shown by the three pressure-volume loops. Source: McCulloch *et al* [18]

### *1.2.2 Myocardial Passive Mechanical Properties*

Constitutive laws used to describe the mechanical behavior of the ventricular myocardium are formulated with material parameters obtained from mechanical testings, such as uniaxial and biaxial tests. Uniaxial tests are very useful for identifying general characteristics of the tissue behavior, but are not appropriate for determining the three-dimensional constitutive behavior of the

myocardium. Biaxial tests, on the other hand, are valuable tools for estimating the myocardial constitutive parameters as they can measure the force and displacement (stress and strain) along orthogonal fiber and cross-fiber axes.

Guccione and coworkers [19] modeled the passive myocardium as a nonlinear, incompressible elastic material and used the following strain-energy function suggested by Fung [20]:

$$W = \frac{C}{2}(e^{Q} - 1) - \frac{1}{2}p(I_3 - 1) \qquad \text{(Eqn 1.1)}$$

where $Q$ is a quadratic function of the strain components, $p$ is a hydrostatic pressure related to the kinematic constraint of constant volume, $C$ is a material constant that scales the overall stresses, and $I_3$ is the third principal invariant of the strain tensor. The kinematic incompressibility constraint is imposed by the relation $I_3 = 1$. For a transversely isotropic material, the following form for Q was used:

$$Q = b_1(E_{11} + E_{22} + E_{33}) + b_2E_{11}^2 + b_3(E_{22}^2 + E_{33}^2 + E_{23}^2 + E_{32}^2) + b_4(E_{12}^2 + E_{21}^2 + E_{13}^2 + E_{31}^2) \qquad \text{(Eqn 1.2)}$$

where $E_{ij}$ are the strain components referring to a system of local muscle fiber (1) in the plane of the wall, cross-fiber in –plane (2), and radial (3) coordinates. $b_1$, $b_2$, $b_3$, and $b_4$ are positive material constants. $b_2$ and $b_3$ are associated with material stiffness along the direction of fiber, in the transverse plane, while $b_4$ is related to the fiber shear in the (fiber, cross-fiber) and (fiber, radial) planes. Isotropy results and the material properties become independent of fiber orientation when $b_2=b_3=b_4$ or when only $b_1$ is nonzero. Several studies have demonstrated that, the stiffness of the myocardial wall is generally higher in the fiber direction than in

the cross-fiber direction in animals [21-23]. In addition, these material constants may vary from one animal or individual to another, resulting in a highly animal- or patient-specific mechanical behavior of the heart.

### *1.2.3 Myocardial Active Mechanical Properties*

Cardiac function is determined largely determined by the integrated effects of mechanical properties of individual cardiac myocytes and connective tissue components. Good understanding of mechanical behavior of the heart and global cardiac function requires a mathematical description for not only the passive mechanical properties of the ventricular myocardium, but also, the mechanics of the active cardiac muscle fibers. A cardiac myocyte, the individual contractile unit of the heart, exhibits a specific activation profile based on its location within the myocardium. Active stresses generated by cardiac muscle fibers are dependent on parameters, such as activation time, shortening velocity, sarcomere length, and intracellular calcium concentration. The active mechanical properties are also patient-specific quantities that may vary from one individual to another. Therefore, parameters, such as the twitch duration scaling factor, the active stress-scaling parameter, and the relationship between time-to-peak tension and sarcomere length need to be estimated in a patient-specific manner. A more detailed description of the mechanics of active cardiac muscle fibers may be found in Guccione and colleagues [19], [24].

## 1.3 Congestive Heart Failure

Congestive heart failure (CHF) is a major cause of morbidity and mortality in the Western societies, which affects more than 5 million people in the United States alone and 23 million worldwide. It is the leading cause of hospitalization for both men and women of age 65 or above in the United States [25] and the number of new cases developing each year in this population has increased in recent years [26]. The healthcare costs associated with CHF, the bulk of which comes from hospitalization costs, are estimated to have been $35 billion in 2008 [27]. CHF is expected to remain as a serious public health problem with high economic impacts on the society, at least in the foreseeable future, with aging of the population as well as modern lifestyles involving unhealthy diets and physical inactivity that pose higher risks for cardiovascular diseases.

Heart failure is a complex clinical syndrome which arises as a consequence of an abnormality in cardiac structure, rhythm, function, or conduction [28]. Heart failure never occurs alone, but is caused by any underlying cardiac defect, such as myocardial infarction, hypertension, dilated cardiomyopathy, degenerative valve diseases, and vitamin B deficiency, which leads to reduced ability of the heart to pump blood. Therefore, a large number of patients with CHF have comorbidity related to the underlying cardiac defect or its cause in addition to the consequences of heart failure. Moreover, the fact that many comorbidities have multiple causes and some others are not completely understood, makes heart failure management highly complex. In general,

decreased efficiency in pump function of the heart in patients with CHF results in reduced blood flow and cardiac output, which cause difficulties in exercising, fatigue, and dizziness. In addition, neurohormonal activation often occurs to increase blood volume by retaining water in the kidneys to compensate for the reduced efficiency in cardiac function. Excess salt and water caused by high blood and fluid pressure backed up behind the heart may also enter the lungs and other body tissues, causing shortness of breath and edema in patients. For effective management of CHF, functional classification that reflects the severity of the condition is necessary. The New York Heart Association (NYHA) Functional Classification provides a scheme for categorizing patients according to the extent of heart failure based on the degree to which they are limited during physical activity (Table 1.1).

**Table 1.1:** NYHA Functional Classification of heart failure.

| NYHA Class | Symptoms |
|---|---|
| **I** | No symptoms of activities and no limitation in ordinary physical activity. |
| **II** | Mild limitation during ordinary activity |
| **III** | Marked limitation even during less-than-ordinary activities. Comfortable only at rest. |
| **IV** | Severe limitations. Symptoms occur at rest |

HF may arise from dysfunction of either the left or right ventricle. It is also typically classified as either systolic or diastolic dysfunction depending on whether the abnormality is caused by contraction or relaxation of the heart. Systolic dysfunction is characterized by reduced ventricular contractility, ventricular dilatation, diminished ejection fraction (EF) and stroke volume (SV),

and increased end-diastolic volume or pressure as a compensation for reduced stroke volume. Diastolic dysfunction often occurs in patients with hypertension and hypertrophy. Although myocardial contractility, diastolic volume and ejection fraction appear to be normal in these patients, an upward shift of the pressure-volume curve and thus, an increase in end-diastolic pressure in the left ventricle are observed since they can no longer accommodate the normal diastolic volume due to the inability of the ventricle to relax. HF is usually accompanied by progressive cardiac remodeling, in which the structure and function of the heart are altered as a compensation of pressure or volume overload and/or cardiac injury. Although remodeling initially occurs as a compensatory change, it will eventually become maladaptive, causing impairment of cardiac function and irreversible injuries.

Currently available treatments of CHF include medications that address the symptoms of CHF and promote myocardial remodeling [29-32], implantable cardioverter defibrillators (ICDs) designed to prevent sudden death due to arrhythmias [33], [34], surgery [35], and transplantation, which is not widely available. Despite these current treatment options, progressively worsening of symptoms in patients with CHF are common and admission rates to hospitals are still high [28]. As of today, heart failure still remains a fatal disease with a survival rate of only 35% five years after patients have been first diagnosed [36]. For this reason, CHF has been the focus of intense research for many years and enormous collaborative efforts have been dedicated by physicians in clinics and scientists in academia to better understand the condition and to develop more

effective heart failure management strategies to help improve the quality of life of patients suffering from this condition.

## 1.4 Cardiac Resynchronization Therapy

Approximately 30% of patients with CHF caused by dilated cardiomyopathy exhibit further complications of HF: an abnormality in the electrical conducting system of the heart known as intraventricular conduction delay. Dilated cardiomyopathy has been found to dramatically increase the risk of mortality when accompanied by intraventricular conduction delay [37]**.** It causes asynchrony of the contraction of the ventricles, leading to a discoordinate wall motion and thus, a much lower efficiency in pumping action of the heart. For example, Left Bundle Branch Block (LBBB), one of the most common types of intraventricular conduction delays seen in patients with dilated cardiomyopathy, results from a blockage or a delay in electrical signal transmission from the *bundle of His* to the left bundle branch and causes a delayed contraction of the left ventricle. A significant recent advancement in the treatment of CHF patients with intraventricular conduction delay has been Cardiac Resynchronization Therapy (CRT) in which ventricular pacing is used to enhance mechanical pump function by restoring synchrony of ventricular contraction. In addition to the two electrode wires common in cardiac pacemakers used to transmit electrical signals from the pulse generator to the right atrium and the right ventricle, the CRT device has a third electrode wire that sends electrical signals to the surface

of the left ventricle. This allows the CRT device to overcome the delay in electrical conduction caused by bundle branch block and simultaneously stimulate both ventricles in order to restore their normal synchronous pumping action.

CRT has been shown in clinical studies to acutely improve cardiac function, lead to beneficial reverse ventricular remodeling in the longer term, increase patient's quality of life, and reduce mortality. However, approximately 30% of patients, especially those with a post-infarct myocardial scar, are classified as non-responders to CRT, who do not gain such benefits from CRT. In addition, variable degrees of benefits observed in responders to the therapy suggest that CRT is often not performed in an optimal fashion. Despite its significant benefits, this is mainly due to a lack of understanding of mechanism of the CRT and a lack of predictive, mechanism-based objective criteria for patient selection, lead placement and pacing protocol. Proper patient selection is crucial as it reduces unnecessary implants, procedural risks and healthcare expenses. However, current patient selection criteria for CRT, such as QRS duration of more than 120 ms, improvements in the distance walked in 6 minutes, peak oxygen utilization ($VO_2$ max) during exercise, and a decrease in left ventricular end-systolic volume, often fail to distinguish responders from non-responders and suggest a need for a more well-defined set of criteria that reflects the mechanism of CRT.

## 1.5 Computational Modeling

Significant opportunities to improve clinical care of CHF have been presented by the quantity and diversity of currently available clinical data. However, developing optimal treatment strategies for patients using this information have not been quite successful. In order to exploit the full potentials of state-of-the-art medical technologies, various types of anatomical and functional information of the patients must be integrated into a consistent framework or a model. *Continuity 6.3*, a problem-solving environment for multi-scale modeling and data analysis in bioengineering and physiology, is an excellent tool for finite element modeling in cardiac biomechanics, biotransport and electrophysiology. It is distributed free for academic research by the National Biomedical Computation Resource and can be downloaded at http://www.continuity.ucsd.edu/Continuity. Finite element method (FEM) is a numerical technique often used in computational modeling of the heart. By discretizing complex 3D geometry of the heart into multiple elements and nodes, FEM solves partial differential equations that govern the mechanical, electrophysiological, and/or electromechanical behavior of the heart. FEM is well-suited particularly for computational cardiac modeling applications that involve domains with complex geometry that constantly change as the heart beats. In addition, FEM allows for an accurate description the anisotropic structure of the myocardial tissue that may influence the global function of the heart. Detailed information about FEM in cardiac modeling can be found in [38] and [39].

While computational models show great potentials to improve clinical care of CHF, models built from population-based metrics derived from different data sets do not always faithfully reproduce or predict the behavior of a specific heart due to individual variability in its response to pathophysiology. Therefore, patient-specific models built from biophysical measurements specific to individual hearts are highly valuable for understanding disease development and therapy benefits that may be different from one to another. The idea of using patient-specific models to predict and optimize the outcomes of CRT has been explored with multiple animal heart models in our group and pacing simulation results from these models have been validated with experimental results [40], [41] .

## 1.6 Goals

Patient-specific computational modeling requires acquisition of various types of data needed to accurately reproduce behavior of the heart. Each of these data sets provides unique information specific to the heart including the three-dimensional geometry, activation sequence, fiber architecture, and mechanical parameters. To build an accurate model, reliable clinical measurements as well as accurate, efficient methods for processing these data sets to extract useful information for model development are needed. Hence, the goal of this study was to design an efficient methodology for developing three-dimensional patient-specific computational models of ventricular electromechanics in the *failing human* heart from various clinical measurements.

The end goal would be to use patient-specific models built using such a methodology to predict and, if possible, optimize the outcomes of CRT. The overall workflow of the study is described in Figure 1.7 and components that are discussed in detail of. Overall, the study is divided into three parts: clinical measurements (blue and green), models, model components or model results (red), and validation of predictions from models (purple). In this thesis, the components highlighted with black are discussed in detail, but with a particular emphasis on methods for modeling some of the most important patient-specific parameters. Methods developed for image segmentation, three-dimensional finite element model development, fiber mapping, endocardial activation mapping, and left ventricular volume estimation are discussed in detail. Furthermore, methods for activation modeling and mechanical parameter estimation are briefly addressed to direct future research.

In the near future, patient-specific models of ventricular electromechanics will be indispensible tools in identifying responders for CRT and optimizing lead placement and pacing protocols. These models will also be used to gain better understanding of the relationship between electrophysiology and mechanics of the heart and answer more fundamental questions of CHF. With sufficiently efficient methods and computational tools for multiscale computational modeling, patient-specific cardiac models will be useful on a large scale in the clinic for surgical planning as well as prediction of surgical and therapeutic outcomes.

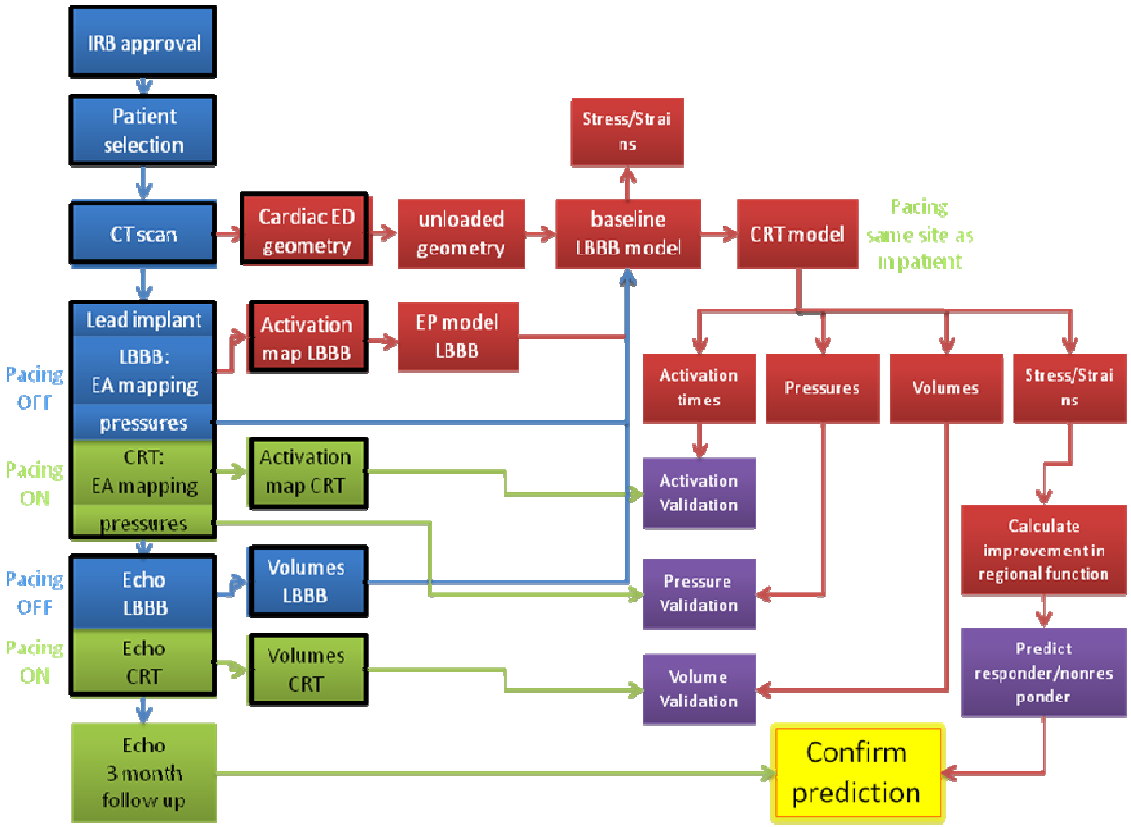


**Figure1.7:** Workflow for design of patient-specific model to predict the outcome of CRT. All baseline measurements of LBBB are shown in blue, all measurements of CRT are shown in green and will be used for validation of the predictions made from patient-specific models. All models, components of models, or model results are shown in red, and validations and predictions are represented in purple. Components highlighted in black are main focus of this thesis. Source: McCulloch 2008 [42]

# Chapter 2

# Materials and Methods

## 2.1 Patient Recruitment and Bi-ventricular ICD Implantation

Upon approval from the Institutional Board of the University of California and Veterans' Affairs Medical Centers, San Diego, a male patient from the Veterans' Affairs San Diego Healthcare System (VASDHS) who had dilated cardiomyopathy with a left ventricular ejection fraction < 35%, New York Heart Association (NYHA) Class III or IV CHF symptoms, and left bundle branch block with a wide QRS complex (> 120 ms) on the surface electrocardiogram (ECG) was studied. The presence of prior myocardial infarction (MI) was documented

by electroanatomical mapping, but was not an exclusion criterion during patient selection. Written informed consent was obtained from the patient.

A biventricular Implantable Cardioverter Defibrillator (Bi-V ICD, St. Jude Medical, USA) was implanted in the patient with the left ventricular lead in a mid-lateral position. The right ventricular lead was implanted in the RV apex, and the right atrial (RA) lead in the right atrial appendage. Immediately after implantation, timing intervals (atrial to RV and RV to LV) were programmed as recommended by the QuickOpt Timing Cycle Optimization algorithm, which calculates appropriate delay settings based on the patient's intracardiac electrograms [43].

## 2.2 Clinical Measurements

### *2.2.1 Cardiac Computed Tomography*

Multi-slice helical CT scans (GE Lightspeed Ultra 8-slice scanner, GE Healthcare Technologies, WI, USA) of the patient were obtained the day before the Bi-V ICD implantation. The imaging technique is summarized as follows: A bolus of non-ionic contrast agent (Omnipague 300, Amersham Health, Oslo, Norway) was injected through an antecubital vein at a rate of 5 mL/second. In a single breath hold, scanning was performed in the cranio-caudal direction at the level of the atrium with simultaneous acquisition of 8 sections per rotation (each section ~1.25mm), beam collimation of 10 mm, table speed of 16.75 mm/0.5 second (0.5 second tube rotation time, 120 kV, 310 mA). Contiguous axial CT

slices of thickness 1.25 mm were subsequently reconstructed and exported in DICOM format.

### *2.2.2 ECG and Left Ventricular Pressure Recordings*

Electrocardiograms (ECG) and intracardiac pressure measurements were recorded using the 160-channel amplifier/recording by Clearsign™ Bard electrophysiologic recorder system (Billerica, MA, USA) at the time of lead implantation for CRT. Signals were acquired at 1000 Hz and subsequently digitized to 16-bit resolution. Intracardiac signals and surface ECG electrograms were bandpass filtered from 30 to 500 Hz and from 0.05 to 100 Hz, respectively. These catheter-based invasive measurements were performed concurrently with electroanatomic mapping described in the next section.

### *2.2.3 Electroanatomic Mapping of Activation Times*

The 3-dimensional geometry of the right (RV) and left ventricles (LV) was reconstructed with the EnSite NavX system (NavX; St Jude Medical), an intracardiac nonfluoroscopic navigation system which has the ability to generate a real-time display showing exact anatomical locations of electrophysiology catheters. The system consists of the Ensite system hardware including the display workstation, patient interface unit and a breakout box, and a specially designed catheter input module. Its three external orthogonal electrode pairs were positioned on the body surface such that 3 orthogonal axes with the heart at the center were formed. The transthoracic electrical field was generated by a 5.68-kHz constant, low-current locator signal that was multiplexed with each pair

of surface electrodes. The potential difference between each catheter electrode and the electrode pairs was measured. Moreover, the catheter electrode positions were determined with a precision of 1mm by measuring changes in potential and impedance that occurred as they moved in the electric field. The 3D endocardial surface geometry was obtained as the physician swept through the ventricles with a mapping catheter that defined the endocardial borders as it made contact with them. Activation timings were measured on the local LV and RV endocardiums with the Bi-V ICD switched on and off. The reconstruction of the endocardial surface geometries and the activation time measurements were both performed at the time of lead implantation for CRT.

### *2.2.4 Transthoracic Echocardiography*

Transthoracic 2D and continuous-wave Doppler echocardiography were performed with standard, commercially available system (Sonos, Philips Medical IE33, Bothell, WA) in order to acquire measurements of ventricular dimensions for volume estimation, fractional shortening, ejection fraction and ratio of early to late diastolic filling(E/A ratio). These measurements were performed after Bi-V ICD implantation and made with the Bi-V ICD switched on. Aortic Velocity Time Integral (VTI) measurements were obtained as outlined by the American Society of Echocardiography guidelines [44]. Same transducer position and sample volume location were maintained during the whole series of atrioventricular (AV)/ paced-to-ventricular (PV) or ventricular-to-ventricular (VV) programming and the optimal AV/PV and VV delay by the echocardiogram method was defined as the

delay associated with the largest average aortic VTI. The VTI echo is used to verify VV delay determined by the QuickOpt Timing Cycle Optimization Algorithm. Aortic Doppler flow velocities were acquired digitally and measurements were obtained after a 1 min delay in order to achieve hemodynamic stabilization.

### *2.2.5 Diffusion Tensor Magnetic Resonance Imaging*

The DTMRI data of a normal excised human heart were obtained from the Johns Hopkins University (JHU) public database: http://www.ccbm.jhu.edu/research/dSets.php. The heart was placed in an acrylic container filled with Fomblin, a perfluoropolyether (Ausimon, Thorofare, NJ) that has a low dielectric effect and minimal MR signal to increase contrast and eliminate unwanted susceptibility artifacts near the boundaries of the heart. The long axis of the heart was aligned with the z-axis of the scanner and images were acquired with a 4-element knee phased array coil on a 1.5 T GE CV/I MRI Scanner (GE, Medical System, Wausheka, WI) using an enhanced gradient system with 40 mT/m maximum gradient amplitude and a 150 T/m/s slew rate at 20 $^{o}$C. Data acquisition was performed with a direct 3D fast spin-echo with 19 diffusion gradient directions and one without diffusion gradient for the normal MRI scan. In order to increase the quality of the image, the acquisition was performed for almost 60 hours. The acquired data were post-processed and arranged in 256×256×134 arrays where each voxel consisted of three eigenvalues and three eigenvectors. The size of each voxel was 429.7μm×429.7μm×1000μm.

## 2.3 Data Processing and Model Development

### *2.3.1 Modeling Three-dimensional Ventricular Geometry*

The ventricular geometry, which has a significant influence on the electromechanical behavior of the heart, varies from patient to patient, and may change due to certain disease conditions such as heart failure. Therefore, in order to develop a three-dimensional multi-scale computational model of ventricular electromechanics in the failing human heart, it is critical to design efficient methods for fitting anatomic meshes that will accurately capture the three-dimensional ventricular geometry that will serve as the computational domain. The procedure involves three major steps: **i)** image segmentation; **ii)** fitting a two-dimensional mesh to data points obtained from image segmentation; and **iii)** generation of three-dimensional cubic elements by making appropriate connections between two-dimensional surfaces.

#### 2.3.1.1 Image Segmentation

The cardiac CT scans of the patient obtained at end-diastole as described previously in section 2.2.1 were manually segmented using ITK-SNAP 1.6.0, a free medical image processing software available for download at http://www.itksnap.org/pmwiki/pmwiki.php. Although ITK-SNAP provides semi-automatic segmentation based on active contour methods, which would yield a more accurate extraction of the ventricular geometry, manual delineation of endocardial and epicardial surfaces in these images was used due to the

presence of several artifacts in this particular set of CT images that made semi-automatic segmentation ill-suited. The procedure for manual segmentation is illustrated in Figure 2.1. Briefly, CT data acquisition was performed at the VA San

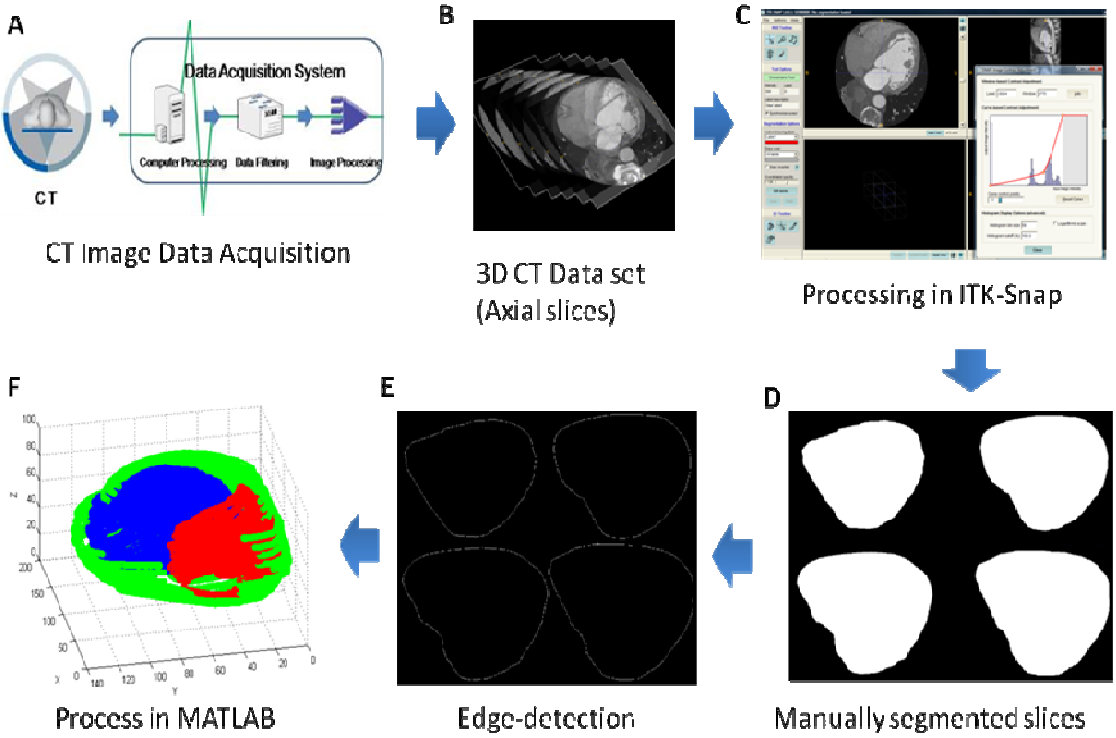


**Figure 2.1:** Overview of the Manual Segmentation process using ITK-SNAP and MATLAB; A)Tranasthoracic CT was performed at the VA San Diego Meidcal Center using an 8-slice CT system; B) The acquired 3D CT data were stored in DICOM format; C) Contrast enhancement was performed to distinguish the cardiac tissues from blood; D) Manual delineation of the endocardial and epicardial surfaces yields a series of binary images; E) Boundaries were extracted by edge detection and; F) imported to MATLAB for further processing.

Diego Medical Center, using an 8 slice CT system as described in section 2.2.1 (Figure 2.1A). The three-dimensional CT data (axial slices) were stored in DICOM format and imported into ITK-SNAP (Figure 2.1B) where contrast

enhancement was performed in order to clearly reveal cardiac tissue structures (Figure 2.1C). Manual delineation of endocardial and epicardial surfaces was performed on approximately 20 slices equidistant from one another from over 130 slices available in the data set, yielding a series of binary images (Figure 2.1 D). Edge detection was performed on the binary images in MATLAB (Mathworks, USA) to extract only the boundaries (Figure 2.1E). The extracted boundary data points from each slice were then prepared for further processing procedures (Figure 2.1F).

The three-dimensional coordinates of the segmented boundary data points representing the surfaces of the left and right ventricles (LV and RV) and the epicardium (EPI) were then further processed such that the actual dimensions were taken into account (voxel size: 0.371 x 0.371 x 1.25 mm). The RV data points were further categorized into either septum (ST) or right ventricular free wall (RVFW) points so that two-dimensional surfaces for ST and RVFW could be fitted independently. Hence, the segmented 3D data points were categorized into LV, ST, RVFW, or EPI. In addition, the coordinate system used in the CT images was modified such that it is consistent with the coordinate system used in Continuity, which has its x-axis along the direction of the long axis of the heart pointing towards the left ventricular apex, and the y- and z- axes in the axial plane where the y-axis intersects the center of RVFW. This was done by a set of rotations that transformed the 3D data points initially represented by the CT image coordinate system into the desired orientation with respect to the Continuity coordinate system. Although this procedure places the data points

roughly in the orientation required for fitting in Continuity, it does not precisely align the long axis of the heart with the x-axis of the coordinate system in Continuity. Procedures needed for such a task is discussed in the next section.

#### 2.3.1.2 Singular Value Decomposition

Successful segmentation of cardiac CT scans of the patient yields a set of data points in the three-dimensional space that represents the boundaries of both ventricles as well as the epicardium of the patient's heart. These data points will be used in Continuity to generate a three-dimensional mesh that accurately represents the patient's unique ventricular geometry. However, such a procedure in Continuity requires that the segmented data points be processed such that the long axis of the heart represented by the data points in three-dimensional space is aligned with the x-axis of the reference Cartesian coordinate system in Continuity. In other words, a method is needed to determine the direction of the long axis of the heart in three-dimensional space. With knowledge of the direction in which the data set is initially aligned and the desired final direction along the x-axis of the reference system in Continuity, it is possible to determine the linear transformation that relates the two. Singular value decomposition (SVD), a mathematical technique based on matrix linear algebra, provides an elegant approach to estimate the long axis of the heart.

In this section, the formal definition of singular value decomposition is presented and its geometrical meaning relevant to this study is discussed briefly.

More in-depth discussions of SVD can be found in [45-47] for interested readers. Given $\mathbf{X} \in R^{m \times m}$, the SVD of a matrix **X** is a factorization of the form

$$X = USV^T \qquad \text{(Eqn 2.1)}$$

where *U* and *V* are $m \times n$ and $n \times n$ orthonormal matrices, and *S* is an $m \times n$ diagonal matrix with the positive singular values $\boldsymbol{\sigma}_j = 1, \ldots, min\,(m, n)$ arranged in descending order along the diagonal. The columns of *U* and *V* are the vectors $\boldsymbol{u}_j$, $j = 1,\ldots,m$, and $\boldsymbol{v}_j$, $j = 1,\ldots,n$. The geometrical meaning of SVD is illustrated using a two-dimensional example of a unit circle ($m=n=2$) in Figure 2.2 When the three factors of SVD are considered separately, $\boldsymbol{V^T}$ serves as a pure rotation, causing the axes $\boldsymbol{v_1}$ and $\boldsymbol{v_2}$ to coincide with the coordinate axes. **S** stretches the unit circle in the directions of the coordinate axes to form an ellipse. Lastly, ***U*** rotates the ellipse into its final position such that the axes $\boldsymbol{v_1}$ and $\boldsymbol{v_2}$ end up as $\boldsymbol{u_1}$ *and* $\boldsymbol{u_2}$, the principal axes of the final ellipse. Same geometrical interpretations apply to three- and higher dimensions.

It is apparent from the geometrical interpretations of SVD that the column vectors $\boldsymbol{u_j}$ of the orthonormal matrix ***U*** computed from SVD of the LV boundary data points represent their principal axes, with $\boldsymbol{u_1}$ in the direction of the largest variance. Ideally, this direction is also the best linear fit of centroids of all LV slices, which corresponds to the left ventricular long axis. Transformations that relate this axis and the basis vector along the direction of the x-axis in the Continuity coordinate system were computed and applied to the entire boundary data set so that it is reoriented along the direction of x-axis (Figure. 2.3). After the

principal axes of the data set were rotated such that $u_1$ was aligned with the x-axis of the coordinate system, the origin was chosen such that it was located at a point two thirds of the apex-to-base distance [49].

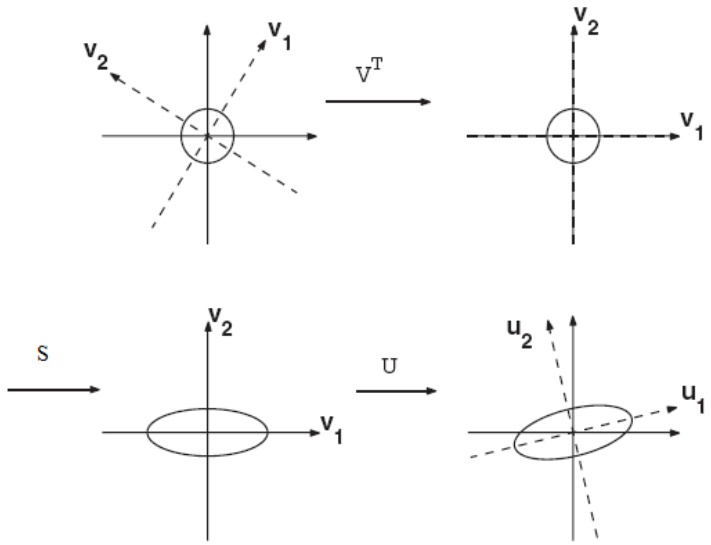


**Figure 2.2:** The geometrical meaning of SVD. Source: Muller *et al* [48]

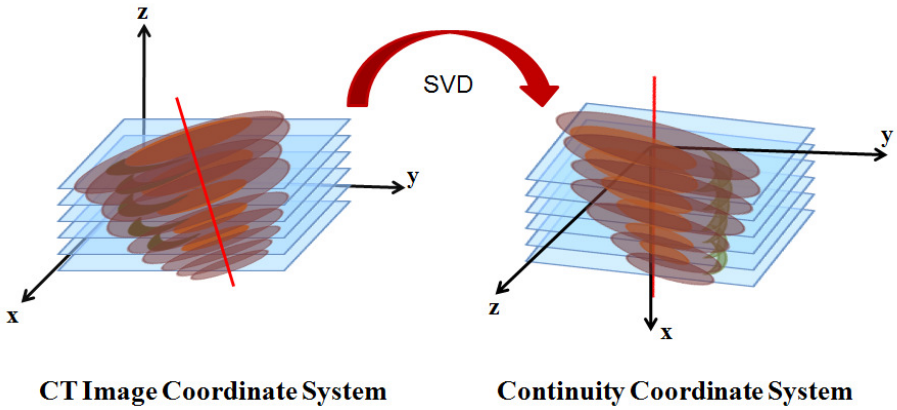


**Figure 2.3:** Transformation from CT image coordinate system to reference coordinate system in Continuity.

#### 2.3.1.3 Two-dimensional Mesh Fitting

**Initial Finite Element Mesh Setup**

In order to generate a geometric model for the heart, finite element modeling technique is utilized. In finite element methods, the geometry of the heart is described by a discretized domain called a mesh with nodes that are connected to form elements. Shape functions defined in local element coordinate systems are used to interpolate the global coordinates of the bordering nodes to calculate the global coordinates of a material point within an element. Therefore, the cardiac geometry can be mathematically expressed using a piecewise polynomial approximation. In other words, the piecewise polynomial function can be fitted to the data points segmented from CT images and processed using MATLAB in the previous section.

Mesh fitting was performed in a prolate spheroidal coordinate system as it is an ideal coordinate system for describing the ellipsoidal nature of the heart: a thick-walled confocal ellipsoidal shell bounded by inner and outer surfaces represented by the dimensional transmural coordinate $\Lambda$ (Figure 2.4).

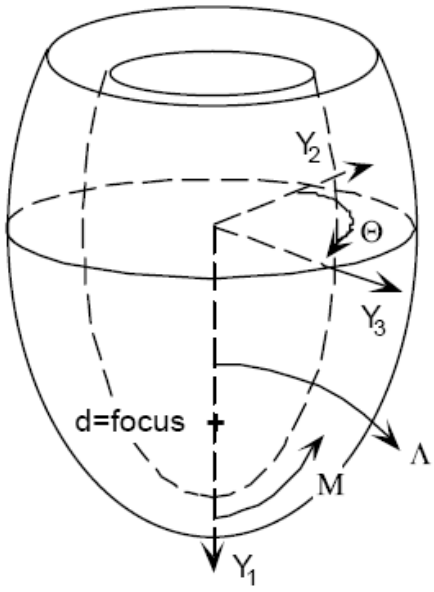


**Figure 2.4:** An ellipsoidal mesh in prolate spheroidal coordinate system (Λ, M, Θ) and its relationship to rectangular Cartesian coordinate system ($Y_1$, $Y_2$, $Y_3$).

Use of a prolate spheroidal coordinate system greatly facilitates the fitting process as it reduces the problem to fitting in Λ direction alone. The relationship between the rectangular Cartesian coordinate system and the prolate spheroidal coordinate system is given by:

$$Y1 = d\cosh\Lambda \cos M \qquad \text{(Eqn 2.2)}$$
$$Y2 = d\sinh\Lambda \sin M \cos\Theta \qquad \text{(Eqn 2.3)}$$
$$Y3 = d\sinh\Lambda \sin M \sin\Theta \qquad \text{(Eqn 2.4)}$$

where the focal length *d* is a parameter used for dimensional scaling of the mesh and is determined by:

$$d^2 = b^2 - a^2 \qquad \text{(Eqn 2.5)}$$

where the major radius b is the distance between the origin and the apex along the x-axis and the minor radius a is the radius at the origin.

In order to generate an accurate finite element model representing the patient-specific ventricular geometry of the failing heart, it is crucial to create an initial finite element surface model that closely resembles the geometry of the heart. The initial finite element surface model consists of two truncated ellipsoids for LV and EPI and two semi-spheroidal surfaces for ST and RVFW (Figure 2.5 and 2.6). Since a sufficient number of nodes and elements is necessary to allow for enough degrees of freedom to achieve accurate fitting results, the initial finite element surface model was constructed with a total of 136 nodes and 116 elements: 8 circumferential elements and 6 longitudinal elements for LV and EPI, and 2 circumferential elements and 5 longitudinal elements for ST and RVFW. The nodal coordinate parameters of bicubic Hermite finite element meshes for LV, EPI, ST, and RVFW were each fitted to a corresponding set of surface data points using the linear least-squares method. Constraints were imposed on the fit such that the derivative symmetry was ensured at the apex and the positions of nodes at RV insertion and the RV apex were kept in place.

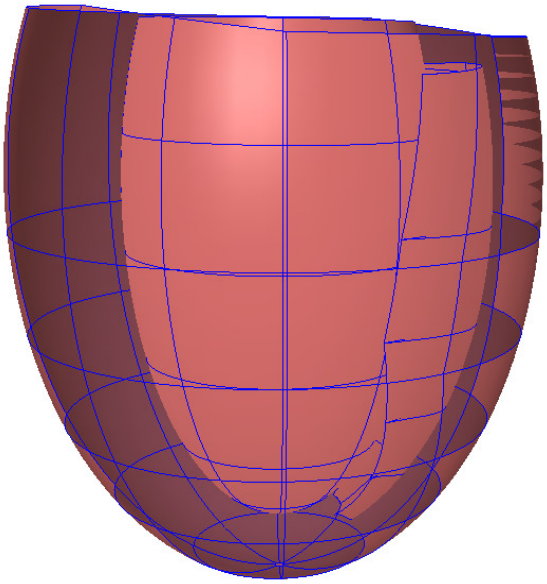

**Figure 2.5:** The initial finite element surface model used for fitting.

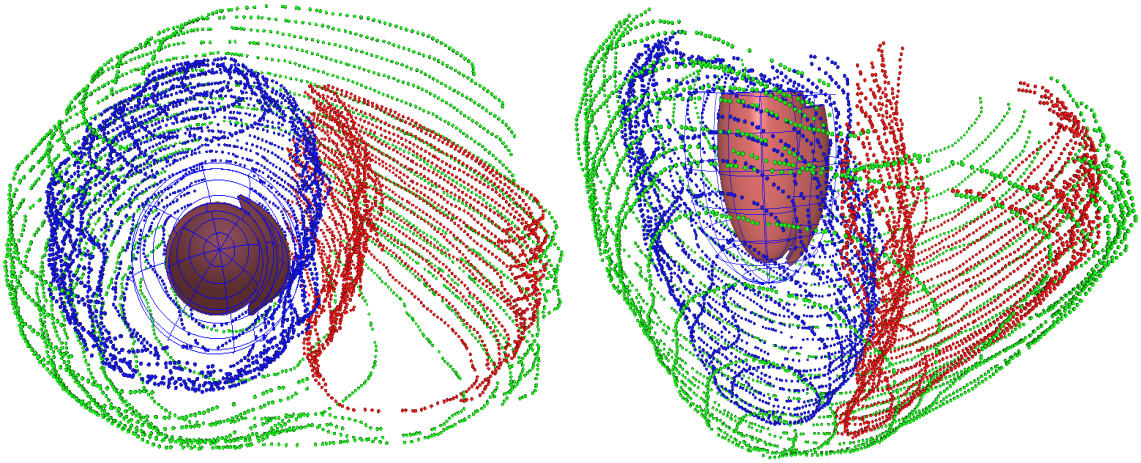

**Figure 2.6:** Top (left) and Anterior (right) views of the initial mesh with data points. LV, RV, and EPI data points are shown in blue, red, and green, respectively.

**Least-squares Fitting for Nodal Geometric Parameters**

Construction of an initial finite element mesh with proper constraints as an initial approximation allows for creating a realistic anatomical model of the ventricular geometry by using the linear least-squares fitting algorithm in Continuity [50]. Briefly, the algorithm computes the best approximations for the nodal coordinates and the derivatives by minimizing the objective function:

$$F(\mathbf{X}) = \sum_{\mathbf{d=1,D}} \gamma_d \left\| \mathbf{X}(\xi_d) - \mathbf{X}_d \right\|^2 + \int_{\Omega} \left\{ \left( \alpha_1 \left\| \frac{\partial \mathbf{u}}{\partial \xi_1} \right\|^2 + \alpha_2 \left\| \frac{\partial \mathbf{u}}{\partial \xi_2} \right\|^2 \right) + \left( \beta_1 \left\| \frac{\partial^2 \mathbf{u}}{\partial \xi_1^2} \right\|^2 + \beta_2 \left\| \frac{\partial^2 \mathbf{u}}{\partial \xi_2^2} \right\|^2 + \alpha_1 \alpha_2 \left\| \frac{\partial^2 \mathbf{u}}{\partial \xi_1 \partial \xi_2} \right\|^2 \right) \right\} d\xi \quad \text{(Eqn 2.6)}$$

where $\mathbf{X}_d$ is the coordinate of the data point and $\mathbf{X}(\xi_d)$ is the interpolated value of, the projection of the data point onto the element surface along the Λ axis. $\alpha_i$ and $\beta_i$ are the fitting weights for the smoothing function and $\gamma_d$ is the smoothing weight associated with each data point. The first term serves to minimize the error between the coordinate of each data point and the corresponding coordinate of the projection on the element surface along the Λ axis. $\gamma_d$ terms were set to one since all measurements were assumed equally accurate. The second term is associated with adjusting the amount of stretch (first derivative terms) and bending (second derivative terms) at the expense of the difference field in the first term. Therefore, the smoothness of the geometric fit depends on

the choice of the fitting weights $\alpha_i$ and $\beta_i$ and thus, it is critical to choose proper values for these parameters.

Based on the empirical data set, the values for $\alpha_1$ and $\alpha_2$ were chosen such that $\alpha_1 = 6\alpha_2$. Furthermore, in order to keep the RMS error minimized, the ratio $\alpha : \beta$ was held constant at 10 [50].

#### 2.3.1.4 Three-dimensional Mesh Generation

The 2D fitted surfaces are composed of a set of 2D elements that are each defined by 4 nodes. 3D tricubic mesh can be generated by redefining the connections between nodes to form 3D elements. Additional nodes were calculated by linear interpolation between the LV nodes and corresponding EPI nodes and were added midway between them to define 3D elements. The basis functions used to define the mesh were changed from bicubic to bicubic-linear in the Λ direction and from bilinear to trilinear in the M and Θ directions in order to calculate new derivatives that would achieve smooth connections between elements. The nodal values and derivatives were converted from prolate coordinate system to Cartesian coordinate system, and the nodes and elements were labeled for subsequent model construction procedures.

### *2.3.2 Modeling Fiber Architecture*

#### 2.3.2.1 DTMRI Background

Diffusion tensor magnetic resonance imaging (DTMRI) is a useful technique for measuring the anisotropic diffusion properties of biological tissues

as a function of spatial position [51]. Previous studies have shown that DTMRI can be used to measure fiber orientations in the ventricular myocardium much more easily and quickly when compared with histological methods that may take up to several months for a single heart [52-54].

In biological tissues such as the ventricular myocardium, the diffusion properties depend on the cellular structure within the tissue. Water molecules can easily move around inside cells, but their movements are restricted by cell membranes. Therefore, it is possible to obtain information about the orientation of cells by studying the measured diffusion properties of biological tissues. For example, in an elongated cell such as the cardiac myocyte, the preferred diffusion direction is along its primary axis. The diffusive properties of the tissues are represented by diffusion coefficients in a symmetric second order diffusion tensor at each voxel,

$$D = \begin{pmatrix} D_{xx} & D_{xy} & D_{xz} \\ D_{yx} & D_{yy} & D_{yz} \\ D_{zx} & D_{zy} & D_{zz} \end{pmatrix} \qquad \text{(Eqn 2.7)}$$

Since the diffusion tensor *D* is symmetric along the principal diagonal (i.e. $D_{xy}$ = $D_{yx}$), it only has 6 independent components.

In order to parametrically morph the fiber architecture of a normal human heart into the patient-specific ventricular geometry, the DTMRI data needs to be processed such that meaningful fiber information in the data set can be properly extracted and fitted in Continuity. The DTMRI data for normal human heart obtained from the Johns Hopkins University public database contains three

orthonormal eigenvectors as well as three eigenvalues associated with each eigenvector for each voxel. The primary eigenvector, which is associated with the largest water diffusion coefficient, is found to be aligned with the fiber direction. Similarly, the secondary and tertiary eigenvectors are aligned with the sheet and sheet-normal directions, respectively. Hence, the primary, secondary, and tertiary eigenvectors form a 3 × 3 matrix, defining a local Cartesian coordinate system for the fiber, cross-fiber, and sheet [55].

For the case of a vector field such as the eigenvectors from the DTMRI data, a tricky problem arises as the positive and negative directions are specified along the current vector when, in reality, the diffusion of water occurs in both directions. In other words, fiber direction is an infinite line in three-dimensional space and thus, multiplying the primary eigenvector by -1 would still be considered the same fiber direction. Although the DTMRI data provide a local basis for each voxel, the distribution of the sign of the basis vectors is random. Therefore, 180-degree rotation of the 3 × 3 matrix consisting of the three eigenvectors will essentially be no different than the original fiber-crossfiber-sheet system. Since incorrect fitting with large gradients of the components of these eigenvectors may result if these 180-degree rotations in the data are not accounted for, it is important to either avoid them in fitting or correct for them before any attempts for fiber fitting are made in Continuity. In this section, a method to avoid problems related to 180-degree rotations that may occur in DTMRI data between neighboring voxels is first presented, followed by a description of subsequent procedures involved in fiber mapping.

#### 2.3.2.2 DTMRI Processing

Although the three eigenvectors are used to define the material coordinate system, direct fitting of the individual vector components as fields is not a valid approach due to the presence of their 180-degree rotations (Figure 2.7). Therefore, instead of fitting individual components of the three eigenvectors, which do not exhibit smooth gradients throughout the myocardial tissue, components of the diffusion tensor can be fitted.

The DTMRI data obtained from the JHU public database was first used to generate another 3D finite element model that represents the unique ventricular geometry of the heart using the procedure described in section 2.3.1. Since the eigenvalues and eigenvectors from the data are simply the results of eigenvalue decomposition of the second order symmetric diffusion tensor *D* that was measured using DTMRI, the diffusion tensor *D* can be easily reconstructed from the given data set as:

$$D = R\Lambda R^T \qquad \text{(Eqn 2.8)}$$

where $D$ = Diffusion tensor
$\Lambda$ = 3×3 matrix with eigenvalues of $D$ as the diagonal entries
$R$ = Linearly independent eigenvectors of $D$ as columns

Since the diffusion tensor *D* is symmetric, its eigenvalues are always real and its eigenvectors are always orthogonal and form a basis. Geometrically, the diffusion tensor *D* can be visualized as a three-dimensional ellipsoid whose axes

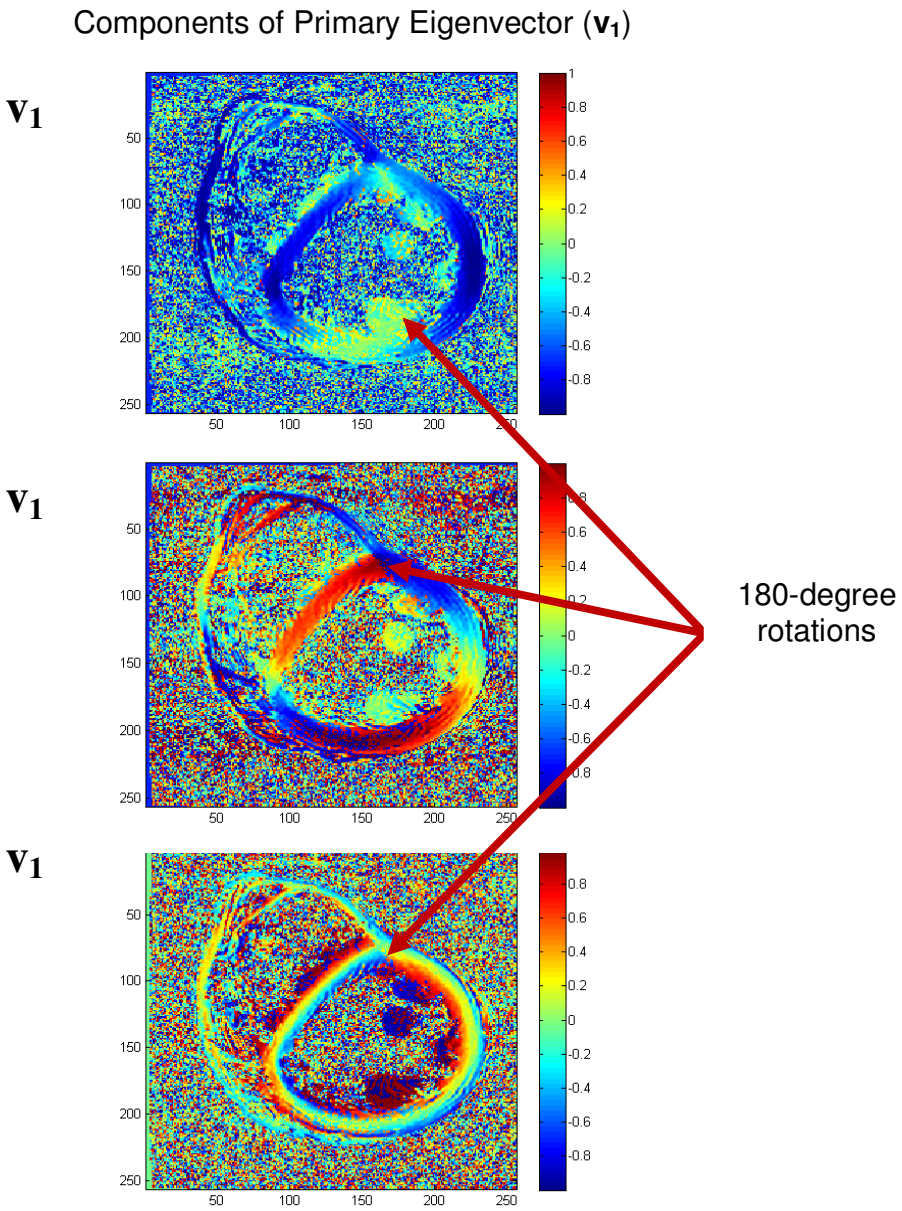


**Figure 2.7:** Images showing the x, y, and z components of the primary eigenvector for slice 50 of a normal human heart. 180-degree rotations are clearly shown as sudden changes in color.

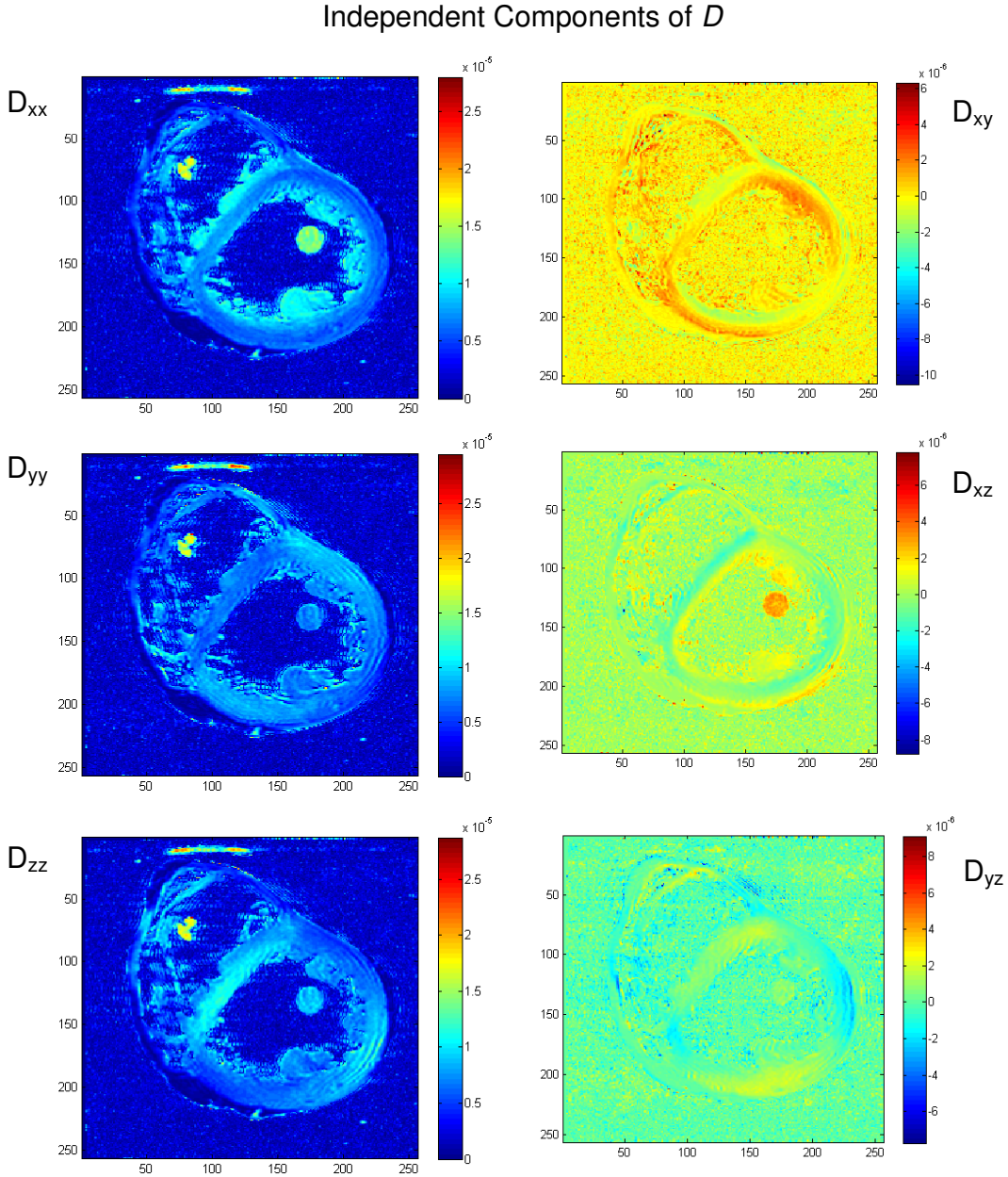


**Figure 2.8:** Images showing the 6 Independent components of the diffusion tensor *D* for slice 50 of a normal human heart. The diagonal components $D_{xx}$, $D_{yy}$, and $D_{zz}$ are shown on the 1st column and the off-diagonal components $D_{xy}$, $D_{xz}$, and $D_{yz}$ are shown on the 2nd column. All 6 components show smooth gradient in both x and y directions and no sudden changes in color is observed.

are aligned with the three eigenvectors associated with the three eigenvalues $\lambda_1 \geq \lambda_2 \geq \lambda_3 \geq 0$. Since $D = R\Lambda R^T = (R')\Lambda(R')^T$, where R' is defined as R that is 180-degrees rotated, the diffusion tensor *D* remains the same regardless of whether the eigenvectors are 180-degress rotated or not. Therefore, the reconstructed diffusion tensor components are always smooth throughout the myocardial tissue as shown in Figure 2.8. The six independent components of the diffusion tensor that correspond to every voxel within the myocardium for 25 slices ranging from slice 1 to 100 were obtained (~430,600data points). The data points were sampled such that only ~71,700 data points were involved in the fitting process. This reduction in the number of data points achieved a significant reduction in computation time without significantly affecting the RMS fitting error. Since a transformation that aligns the long axis of the boundary data points with the x-axis in Continuity was applied before constructing the 3D finite element mesh that models the ventricular geometry, the exact same transformation was performed on the data points with diffusion tensor components from the DTMRI data. The same transformation was also applied to the diffusion tensor *D* as well so that the principal direction of water diffusion is preserved for a given location within the myocardium. Since the coordinates of a data point can be represented by a vector, they were pre-multiplied by a transformation matrix **T** to yield their new coordinates (i.e. v'=**T**v). However, tensor transformation involves both pre- and post-multiplication by the same transformation matrix applicable to vector transformation (i.e. $D' = \mathbf{T}D\mathbf{T}^{\mathbf{T}}$). Therefore, the diffusion tensor *D* was pre- and post-multiplied by the transformation matrices used to transform the boundary

data points from the image coordinate system to the coordinate system in Continuity with their long axis aligned with the x-axis.

#### 2.3.2.3 Fiber Mapping

Each of the 6 independent components of the diffusion tensor was fitted individually using trilinear basis functions in Continuity without the use of any smoothing weights since there was a sufficient number of data points evenly distributed throughout the 3-D finite element mesh which served as the computational domain (Figure 2.9). Any data points that did not reside within this computational domain were automatically detected and ignored during calculation.

The fitted values and their derivatives were stored in the nodes as fields, and were subsequently interpolated into Gauss points where eigenvalue decomposition was performed. The eigenvalues and the corresponding eigenvectors were computed at Gauss points and were used to calculate the nodal parameters again. By performing eigenvalue decomposition at the Gauss points rather than at the nodes, orthonormality of the resulting eigenvectors is ensured. The eigenvalue decomposition procedure still results in a random distribution of sign of eigenvectors and leads to 180-degree rotations. However, this is no longer an issue since the problem of fitting eigenvector components that have large gradients has been bypassed by using this method and 180-degree rotations that may result from eigenvalue decomposition at Gauss points are treated equally as eigenvectors with no rotations.

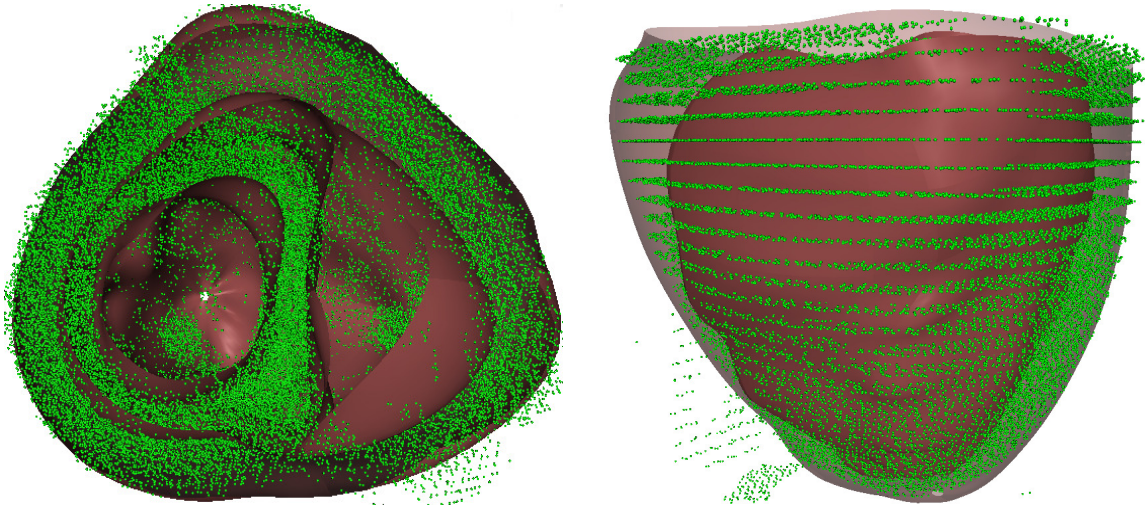

**Figure 2.9:** Geometric 3D finite element model of the normal human heart from the DTMRI data from JHU public database and data points where diffusion coefficients were measured (green).

The method was tested and validated on a single cubic element of size 1 x 1 x 1unit, with synthetic data. Eigenvectors were created at a total of 396 locations within the element (6 × 6 × 11 points) such that the fiber angle, defined as the angle between the primary eigenvector and the horizontal plane, made a linear variation from $+50^{o}$ on the front surface to $-50^{o}$ on the back surface of the element (Figure 2.10). The fiber angles were set constant in the remaining two directions. $180^{o}$ rotations of the eigenvectors were introduced in the synthetic data set by selecting data points at random within the element and rotating the orthogonal set of eigenvectors associated with the data point 180 degrees about the z-axis. Eigenvalues were created such that $\lambda_1$ was the largest and $\lambda_3$ was the smallest ($\lambda_1$=1, $\lambda_2$=0.5, and $\lambda_3$=0.2). The diffusion tensor was constructed for

each data point from the synthetic eigenvectors and eigenvalues as previously described and its 6 independent components were fitted. To investigate the effects of different basis functions as well as the number of elements used in fitting, trilinear basis functions and linear-linear-cubic basis functions were tested on a single cubic element and a two-element mesh obtained from refining the single cubic element in the direction perpendicular to the front surface (transmural). Finally, eigenvalue decomposition was performed to calculate the eigenvectors at any point within the element.

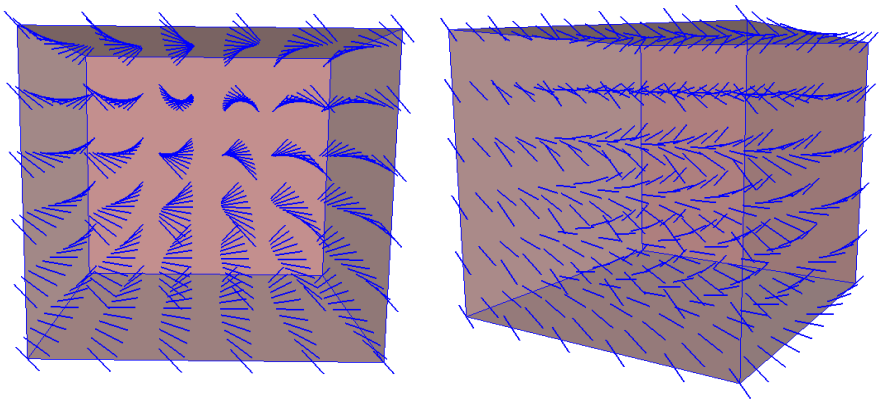

**Figure 2.10:** A cubic element and synthetic data used to test the fiber mapping method. Eigenvectors were generated such that the fiber angle linearly varied from -50$^{o}$ on the front surface to 50$^{o}$ on the back surface. The primary eigenvectors are rendered (in blue), showing the linear change in fiber angle across the wall.

### 2.3.3 Endocardial Activation Time Fitting

Electroanatomic endocardial activation time measurements of both ventricles were obtained in succession, with the Bi-V ICD turned on and off as described in Section 2.2.3. The electroanatomic map was displayed as a spatial representation of activation times. Therefore, the data consisted of 3D

coordinates of electrode position within the ventricular cavities and corresponding activation times and membrane voltages. The time points that corresponds to the peak of the QRS complex in the surface ECG was used as the reference during the post-processing procedure before exporting from the electroanatomic mapping system since it is the easiest point to detect on an ECG recording.

The 3D surface geometry generated by the electroanatomical mapping system is largely different from the ventricular geometry dictated by the 3D finite element model constructed from segmenting MRI or CT data. This problem is caused by the fact that the 3D surface geometry is created based on the locations of the data points obtained using a mapping catheter. Complex geometry and anatomical structures within the ventricular cavities often impose restrictions on freedom of movement of the mapping catheter and do not allow accurate reconstruction of the anatomic details of the ventricular surface geometry. Moreover, the surface geometry is obtained randomly throughout the cardiac cycle, but not at a specific ECG-gated time like end-diastole or end-systole. Use of an inaccurate geometry as a domain for electroanatomical mapping might also give false ideas about the activation pattern mapped out by the system. Therefore, in order to accurately represent the endocardial activation pattern, it is crucial to assign each data point to its correct anatomic location in the 2D finite element model of the failing heart created in section 2.3.1.

To align the data points with the 2D finite element model, SVD was performed on data points taken from the LV endocardial surface as described in section 2.3.1.2. The whole data set (both LV and RV data points) was tilted such

that the x-axis in Continuity's coordinate system passed through the centerline of the LV data points and was scaled appropriately based on the dimensions of the ventricles (Figure. 2.11). Each data point was then projected onto the closest point on the endocardial surfaces of LV or RV, but those that are sufficiently far away from the surfaces were ignored. Once projected, activation times for LV and RV endocardial surfaces were each fitted as fields after they were adjusted such that the earliest activation occurred at t = 0. Different smoothing weights were explored to obtain optimal fitting result. The endocardial activation maps obtained from fitting were transferred to the 3D finite element model. These activation maps on the endocardial surfaces of the 3D model serve as initial conditions to estimate the activation times across the ventricular walls.

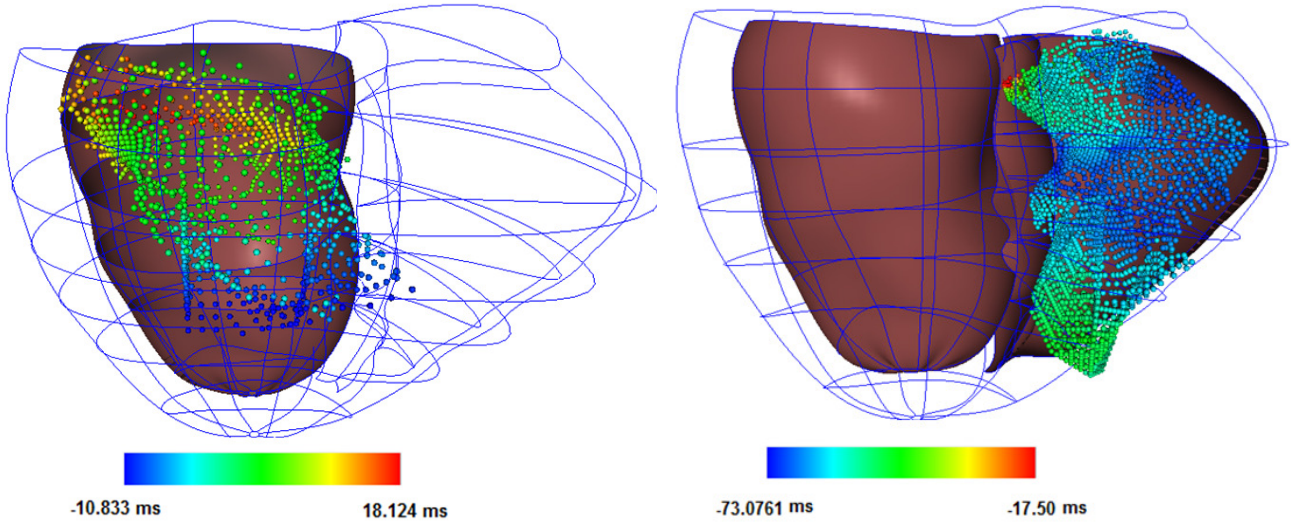


**Figure 2.11** Activation time data points rendered on LV (left) and RV (right) endocardial surfaces.. The data points were aligned with the long axis of the model and were scaled in x, y, and z directions based on the dimensions of the ventricles. The activation time measurements were color-coded.

### 2.3.4 Estimation of Left Ventricular Cavity Volumes

The passive and active material properties in the model of cardiac mechanics as well as circulatory model parameters can be estimated by using the dynamic ventricular volumes and pressures obtained from 2D transthoracic echocardiography and LV pressure recordings, respectively. From the 2D echo images, the endocardial outline was manually traced and the axial length of the chamber L, which was defined as the line between the LV apex and the mid-point of the aortic valve, was subdivided into segments $\Delta L$. The LV volume $V$ was approximated using single-plane Simpson's method [56], as the summed volumes of graduated circular discs with diameter $D_i$ and thickness $\Delta L$:

$$V = \sum_{i=1}^{n} \frac{\pi}{4} D_i^2 \Delta L \qquad \text{(Eqn 2.9)}$$

The LV volumes were also estimated using biplane Simpson's method, which in theory, should provide more accurate results with information about LV dimensions obtained two different views. In the biplane Simpson's method, the discs are now assumed to be elliptical with a major radius A and a minor radius B:

$$V = \sum_{i=1}^{n} \pi A_i B_i \Delta L \qquad \text{(Eqn 2.10)}$$

This method may be performed to estimate LV volumes at any time point through the cardiac cycle including end-systole and end diastole.

# Chapter 3

# Results

## *3.1 Cardiac Computed Tomography and Image Segmentation*

Contiguous axial CT slices of thickness 1.25 mm were obtained (Voxel size: 0.371 x 0.371 x 1.25 mm) from the multi-slice helical CT scanner and exported as a DICOM format (Figure 3.1). The results of the manual delineation of endocardial and epicardial surfaces in the CT slices are shown in Figure 3.2.

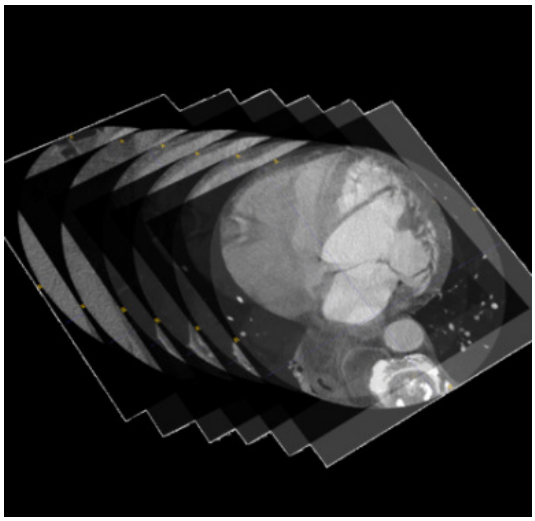

**Figure 3.1:** Contiguous axial CT slices of voxel thickness 1.25mm. Only a few out of over 130 slices are shown.

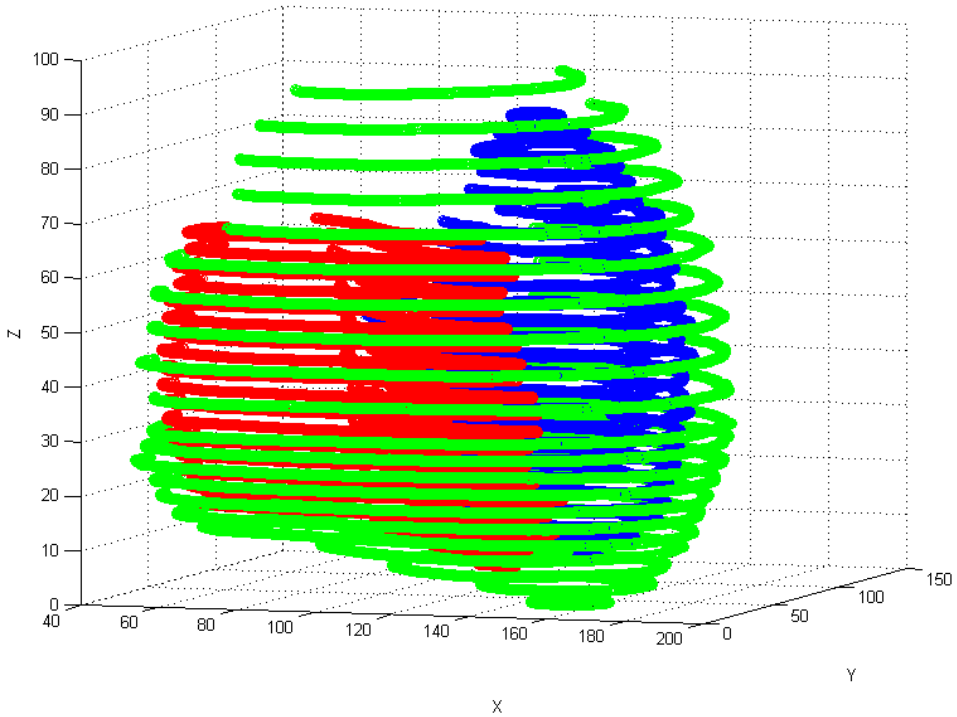


**Figure 3.2:** Endocardial and epicardial boundary contours manually delineated from the axial CT slices (blue: LV, red: RV, green: EPI).

## 3.2 Singular Value Decomposition and Geometric Model Development

SVD was performed on the LV data points to determine the direction of the largest variance. Transformations were applied to the data points such that this direction, which, in theory, is the center axis of the LV or the long axis of the heart, is aligned with the x-axis of the Continuity coordinate system. As shown in Figure 3.3, results from SVD of LV boundary data points in their original configuration (black) were used to compute the transformations required to align the data points along the x-axis of the Continuity coordinate system (yellow). The same transformations were applied to the ST, RVFW, and EPI data points so that the entire data set was aligned (Figure 3.4)

Various combinations of smoothing weights were explored to obtain the best-fit 2D finite element model as described in section 2.3.1.3 and the resulting RMS fitting errors are plotted (Figure 3.5). The RMS fitting error increased slowly for values of $\alpha$ less than 0.1 and more rapidly for higher values of $\alpha$. The elbow of the curve at $\alpha = 0.1$ corresponded to an RMS fitting error of 1.294 mm, which is comparable to the voxel thickness of 1.25 mm. By using $\alpha = 0.1$ as the smoothing weight, a substantial improvement in the smoothness of the fitted mesh was observed with a negligible amount of increase in the RMS fitting error. Therefore, $\alpha = 0.1$ was used to fit the 2D initial finite element surface model to the data points. More detailed descriptions of effects of smoothing weights can be found in Mazhari et al 1998 [50].

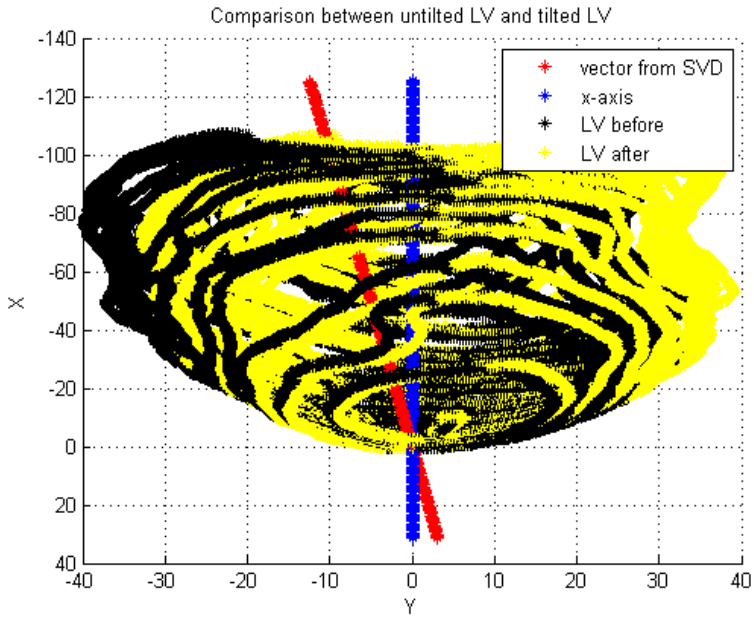


**Figure 3.3:** Comparison between the LV boundary data points in their original configuration (black) and after transformations were applied (yellow). The primary axis of the data set computed from SVD and the x-axis of the Continuity coordinate system are shown in red and blue, respectively.

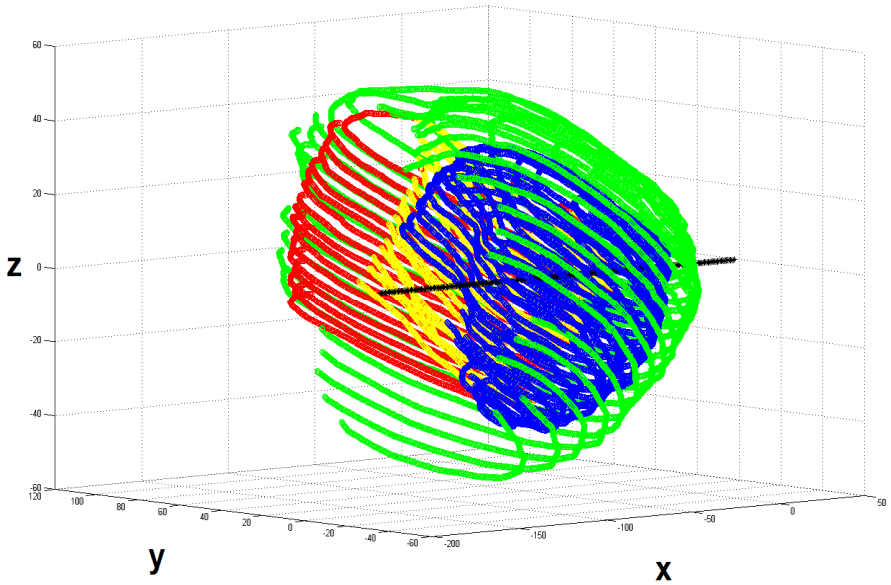


**Figure 3.4:** Boundary data points of all anatomic structures (blue: LV, yellow: ST, RVFW: red, and green: EPI) after transformations were performed. The x-axis shown in black passes through the center line of the LV data points.

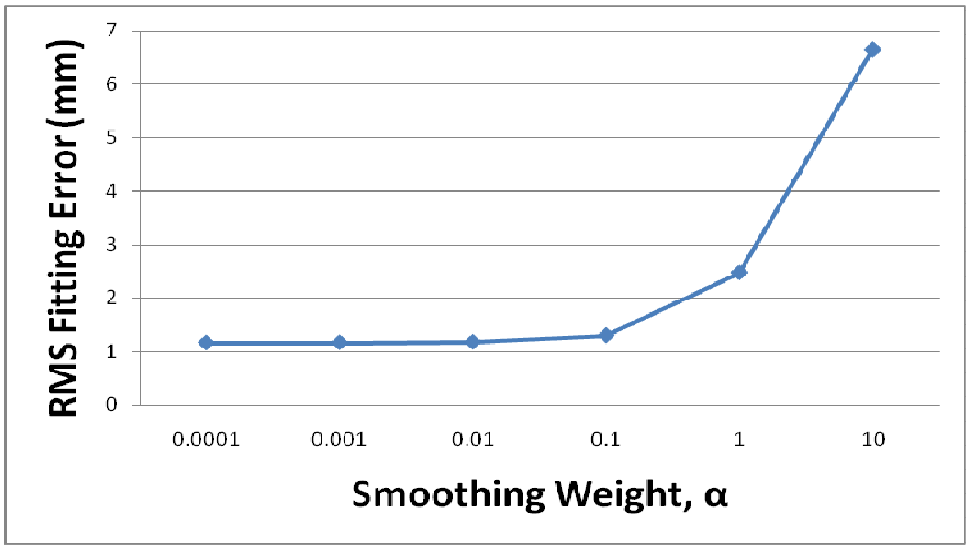


**Figure 3.5:** Effect of the smoothing weight, α on the RMS fitting error.

The resulting 2D mesh had smooth surfaces that accurately represent the ventricular geometry of the failing heart (Figures 3.6 and 3.7). Finally, the 3D finite element model built from the 2D mesh by redefining the basis functions and nodal connections for 3D cubic elements with additional nodes between epicardial and endocardial nodes is shown in Figure 3.8. The 3D tricubic mesh consisted of 2 elements in the axial direction (across the myocardial wall) around the LV free wall and 1 element for the septum and the RV free wall, totaling 120 tricubic elements and 232 nodes (8 nodes per element).

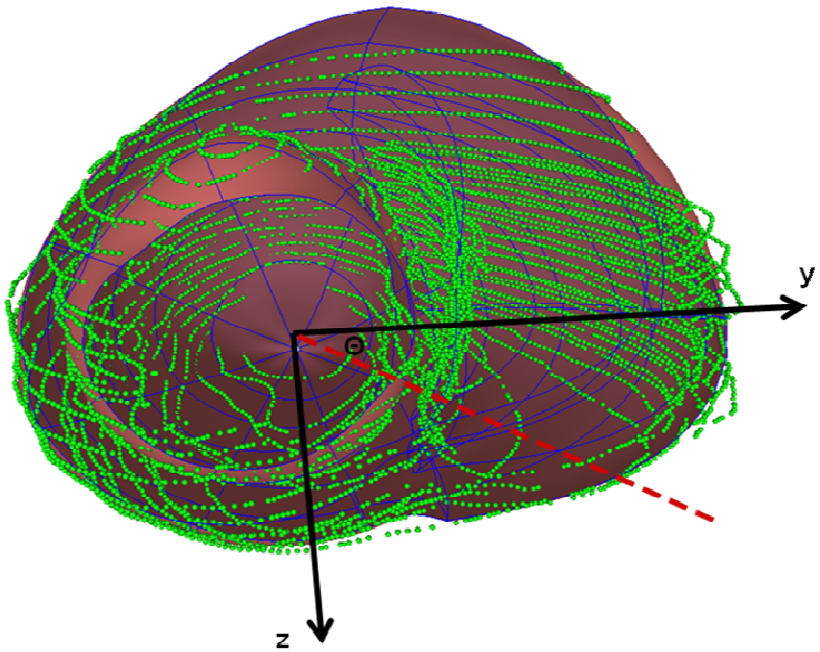


**Figure 3.6:** Top view of the 2D mesh fitted to the data points (in green).The reference coordinate system in Continuity is shown with black axes.

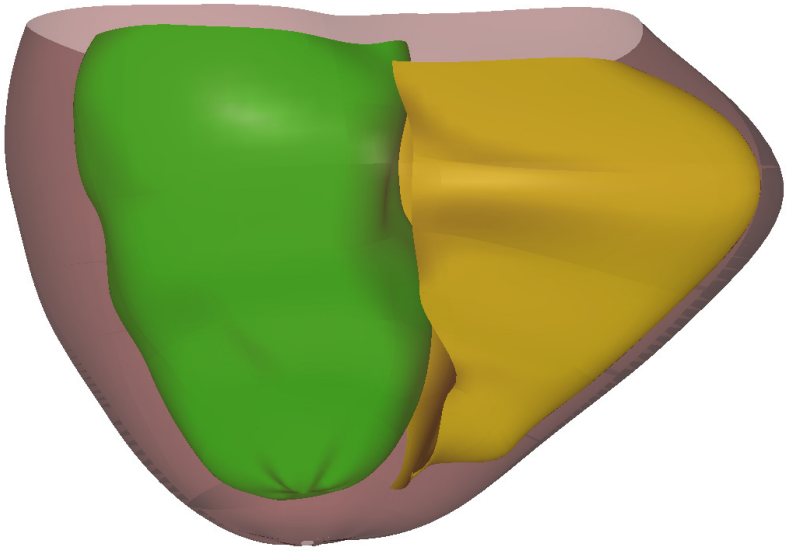

**Figure 3.7:** Posterior view of the 2D finite element surface model.

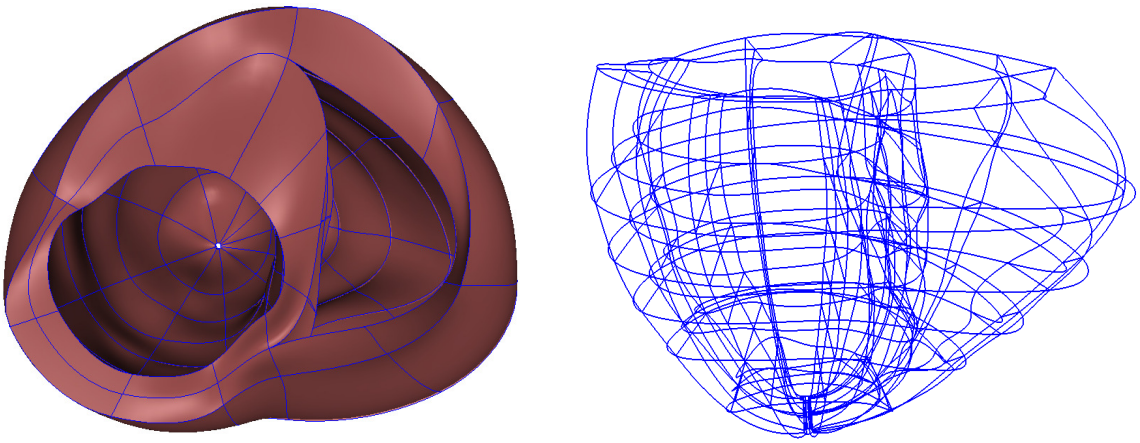

**Figure 3.8:** 3D finite element model of the failing heart: a) Top view with its surfaces and element lines rendered. b) Posterior view with its elements lines rendered.

## *3.3 DTMRI Processing and Fiber Mapping*

The method developed for fiber mapping from DTMRI data was tested on a cubic mesh with synthetic data. The eigenvectors computed from eigenvalue decomposition of the fitted diffusion tensor components were rendered at the same locations as the data points and were compared with the original synthetic eigenvectors at these locations. Different combinations of basis functions and number of elements were explored and their RMS fitting errors are presented in Table 3.1. Generally, refinement of the cubic element in the direction of fiber angle gradient (i.e. transmural direction) resulted in lower RMS fitting errors. In addition, Linear-Linear-Cubic basis functions, which use a cubic interpolation function in the direction of fiber angle gradient, yielded much lower RMS fitting errors for a given number of elements. The fiber mapping results for single and

two-element cubes with trilinear basis functions are shown in Figure 3.9 and 3.10, respectively.

**Table 3.1:** RMS fitting errors for diffusion coefficients using different basis functions and number of elements.

| | **Trilinear** | | **Linear-Linear-Cubic** | | |
|---|---|---|---|---|---|
| | **1 element** | **2 elements** | **1 element** | **2 elements** | **Range** |
| $D_{11}$ | 0.1036 | 0.0309 | 0.0081 | 0.0007 | [0.5000 0.7934] |
| $D_{12}$ | 0.0345 | 0.0426 | 0.0014 | 0.0005 | [-0.2462 0.2462] |
| $D_{13}$ | 0.0000 | 0.0000 | 0.0014 | 0.0000 | [0 .0000 0.0000] |
| $D_{22}$ | 0.1036 | 0.0309 | 0.0081 | 0.0007 | [0.7066 1.0000] |
| $D_{23}$ | 0.0000 | 0.0000 | 0.0000 | 0.0000 | [0.0000 0.0000] |
| $D_{33}$ | 0.0000 | 0.0000 | 0.0000 | 0.0000 | [0.2000 0.2000] |

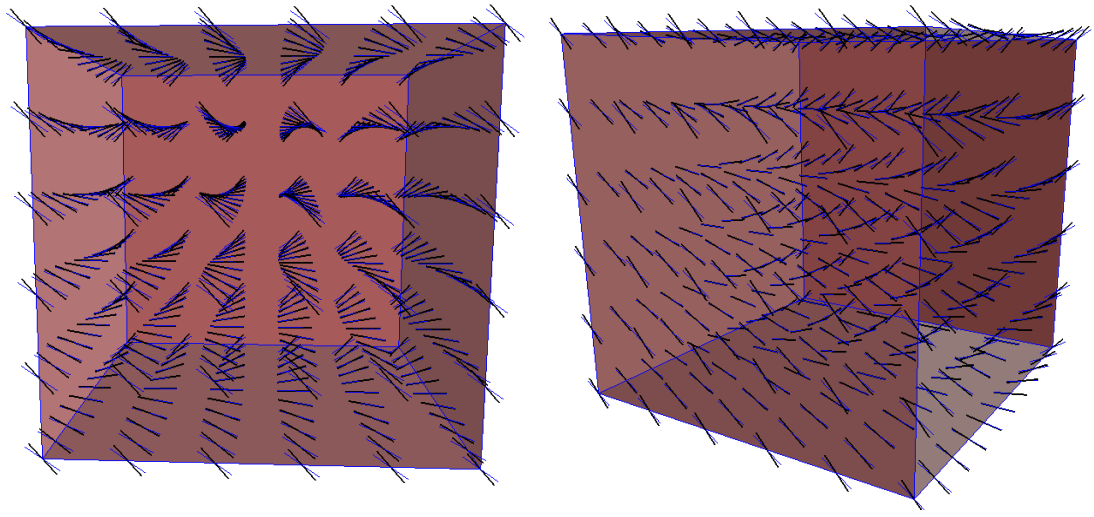

**Figure 3.9:** Fiber mapping results with trilinear basis functions on a single cubic element. The eigenvectors from the data are shown in black and the eigenvectors computed from eigenvalue decomposition are shown in blue.

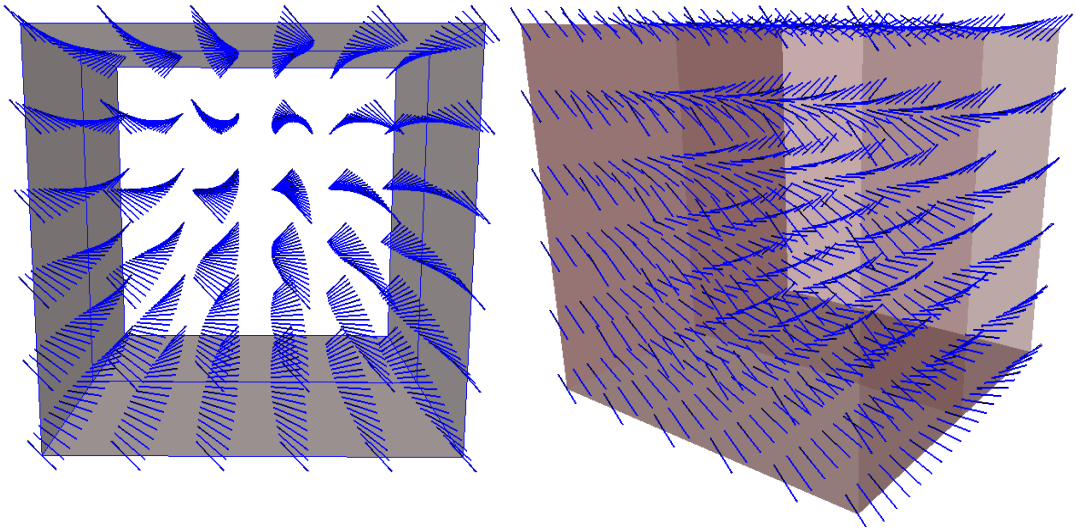

**Figure 3.10:** Fiber mapping results with trilinear basis functions on a two-element cubic mesh. The eigenvectors from the data are shown in black and the eigenvectors computed from eigenvalue decomposition are shown in blue.

The effects of errors introduced in fitting of the diffusion coefficients on fiber angles were investigated by computing fiber angles from the resulting eigenvectors at Gauss points within the element. The fiber angles are plotted as a function of normalized transmural position (back surface = 0 and front surface = 1) as shown in Figure 3.11. As summarized in Table 3.2, using trilinear basis functions and a 1-element cube resulted in an RMS error of 6.40 degrees and a maximum absolute difference of 7.89 degrees between fiber angles from the synthetic data and those computed using the proposed method. Significantly better results were obtained with 2-element cube with linear-linear-cubic basis functions. The RMS error was only 0.07 degrees and the maximum absolute difference in fiber angles was only 0.10 degrees. This suggests that at least 2 elements in the transmural direction with linear-linear-cubic basis functions are

needed to achieve high accuracy in mapping the fibers from DTMRI data to the model.

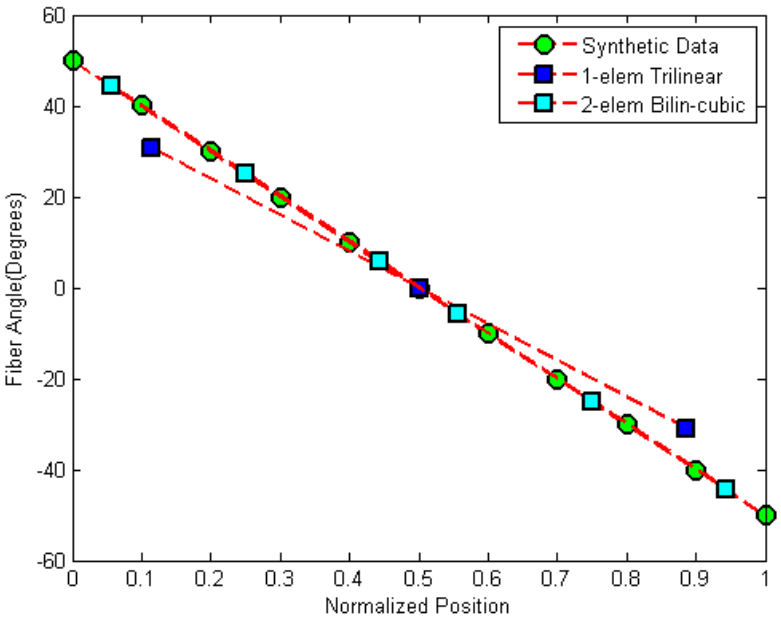


**Figure 3.11:** Comparison between fiber angles from synthetic data and those computed from eigenvectors as a result of eigenvalue decomposition at Gauss points. Fiber angles are shown as a function of normalized transmural position (back surface = 0 and front surface = 1) for the synthetic data (green), 1-element trilinear case (blue), and 2-element linear-linear-cubic case (magenta). The synthetic data consisted of diffusion coefficients derived from eigenvectors that increased linear from -50$^o$ on the front surface to +50$^o$ on the back surface of the cube. Some of these eigenvectors were rotated 180 degrees to mimic the large gradients of eigenvector components in real DTMRI data.

**Table 3.2:** RMS errors and maximum absolute differences between fiber angles from synthetic data and those computed from different combinations of basis functions and number of elements for fitting diffusion coefficients.

| | Trilinear basis fcns | | Bilinear-Cubic basis fcns | |
|---|---|---|---|---|
| | 1 element | 2 elements | 1 element | 2 elements |
| RMS Error | 6.40$^o$ | 1.69$^o$ | 0.86$^o$ | 0.07$^o$ |
| Max. Abs Difference | 7.89$^o$ | 2.05$^o$ | 1.06$^o$ | 0.10$^o$ |

The proposed fiber mapping method, which was verified using a cubic element with synthetic data, was then applied to map cardiac fibers on the 3D finite element model constructed from the DTMRI data. Fiber orientations throughout the entire ventricular myocardium are represented by primary eigenvectors from DTMRI data as shown in Figure 3.12. The second-order symmetric diffusion tensor *D* was reconstructed from the eigenvectors and eigenvalues for a normal human heart provided by the JHU public database. Each of the 6 independent components of the diffusion tensor was fitted individually without any smoothing weights and their corresponding RMS fitting errors are shown in Table 3.3. The diffusion coefficient range is wider for the diagonal components $D_{11}$, $D_{22}$, and $D_{33}$ than the off-diagonal components $D_{12}$, $D_{13}$, and $D_{23}$. Therefore, the RMS fitting errors for the diagonal components are typically a few times larger. Next steps include computing the eigenvectors from the diffusion tensor constructed from the fitted diffusion coefficients and comparing them with the original DTMRI data.

**Table 3.3:** RMS fitting errors for diffusion coefficients and their ranges.

| Diffusion Coefficients | RMS Fitting Error ($\times 10^{-6}$ mm$^2$/s) | Diffusion Coefficients Range ($\times 10^{-6}$ mm$^2$/s) |
|---|---|---|
| $D_{11}$ | 1.2926 | [0.0090 21] |
| $D_{12}$ | 0.4768 | [-5.930 6.21] |
| $D_{13}$ | 0.4440 | [-8.30 7.18] |
| $D_{22}$ | 1.3628 | [0.0182 25.7] |
| $D_{23}$ | 0.4817 | [-8.640 5.41] |
| $D_{33}$ | 1.3296 | [0.0103 23.7] |

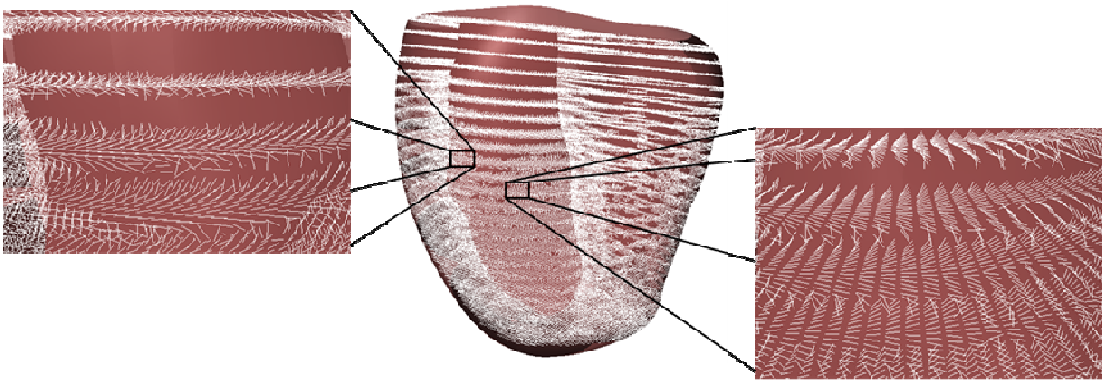

**Figure 3.12:** 3D finite element model of the normal human heart from JHU DTMRI data, showing the fiber orientation with primary eigenvectors throughout the myocardium. Two regions, one on the left ventricular free wall and the other on the posterior wall of the left ventricle, are enlarged to demonstrate the transmural variation of the fiber orientations.

## *3.4 Endocardial Activation Time Mapping*

Local activation times were measured on the LV and RV endocardium using Ensite NavX system and the isochronal maps of LV and RV were constructed (Figure 3.13). The number of measurements taken and the range of activation times are shown in Table 3.4. Due to its complex anatomical structures and dimensions, the number of measurements taken from LV was much smaller than that of RV.

**Table 3.4:** Local Activation Time measurements in LV and RV with t =0 at the peak of QRS complex.

| | **# of Measurements** | **Activation Time (ms) [apex base]** |
|---|---|---|
| **LV** | 1240 | [-54.2 90.6] |
| **RV** | 3158 | [-73.1 -17.5] |

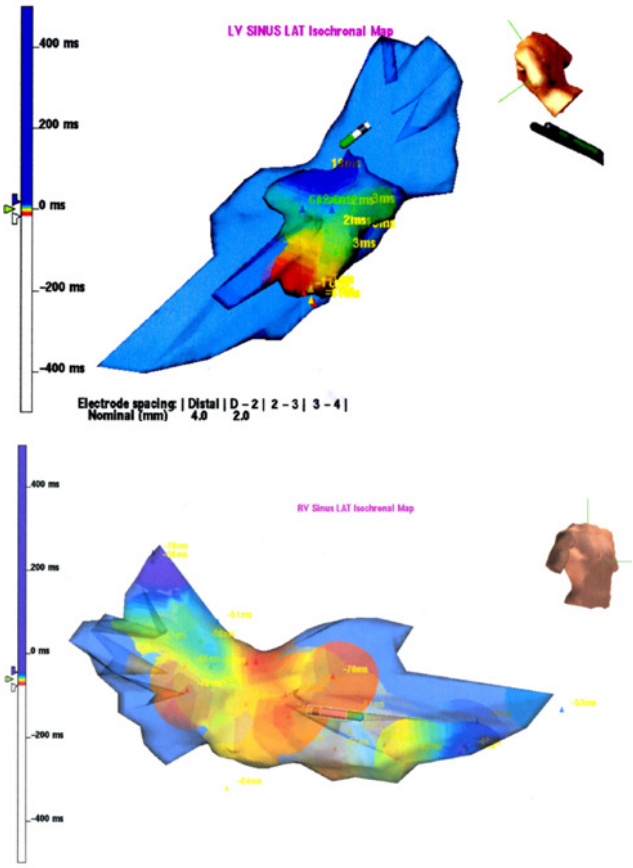


**Figure 3.13:** Isochronal maps of LV (Top) and RV (Bottom) activation times generated by Ensite NavX system.

The endocardial activation time fitting results are shown in Figures 3.14 and 3.15. Fitting was performed after the data points were scaled and projected on the endocardial surfaces of the ventricles. Different magnitudes of smoothing weights were explored and their effects on RMS fitting error were investigated. In order to obtain best fitting results, $\alpha = 0.1$ was used for both LV and RV and their corresponding RMS fitting errors were 0.927ms and 1.148 ms, respectively, which corresponded to the elbow of the curve in Fig 3.16. The nodal values and

derivatives that describe the endocardial activation pattern on a 2D surface model were transferred to corresponding nodes in the 3D FE model (Figure 3.17).

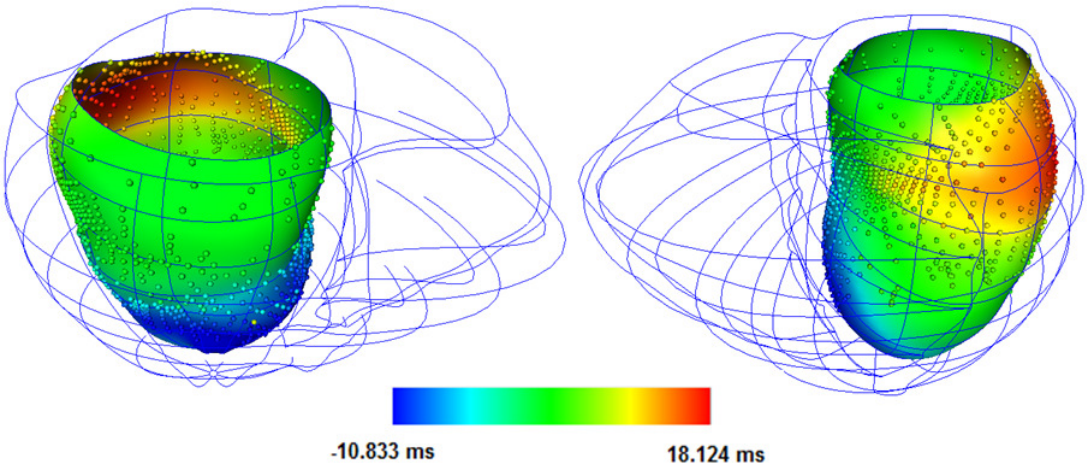


**Figure 3.14:** Activation time data points projected and fitted on the LV endocardial surface: left (Posterior view) and right (Anterior view).

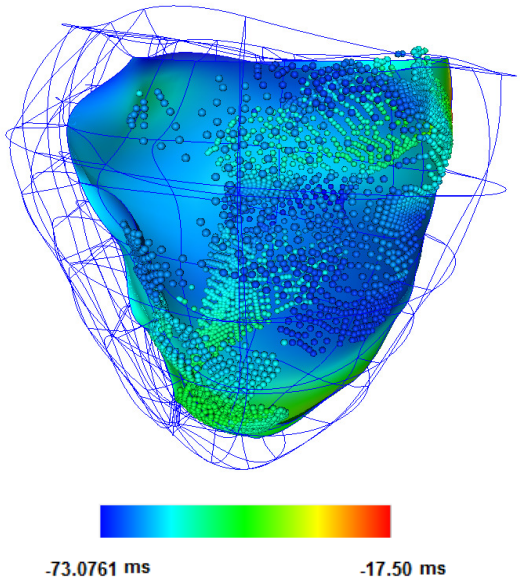


**Figure 3.15:** Activation time data points projected and fitted on the RV endocardial surface.

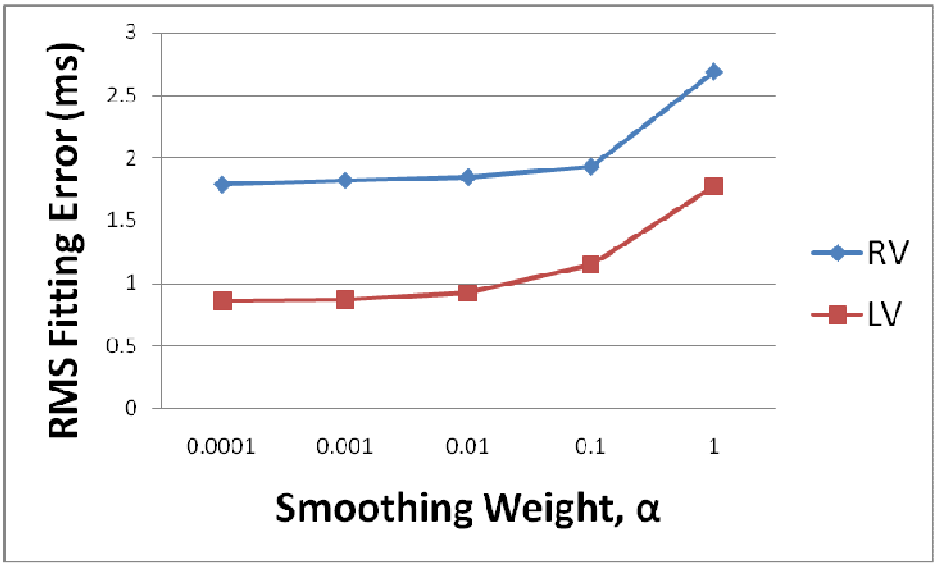


**Figure 3.16:** Effect of smoothing weight on RMS fitting errors for LV and RV endocardial activation time fitting.

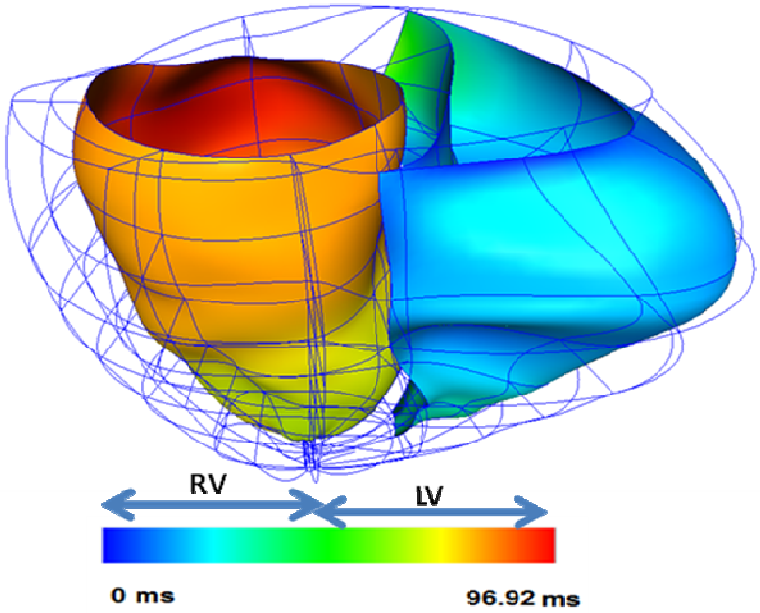


**Figure 3.17:** Endocardial activation time map transferred from 2D to 3D finite element model.

## *3.5 Dynamic Ventricular Volumes and Pressures*

The 2D transthoracic echocardiograms of the patient's heart were recorded in real-time at 33 frames per second with Bi-V ICD turned on and pacing both the atria and ventricles at 70 bpm. Ideally, echocardiograms with Bi-V ICD turned off are needed as well, but they were not obtained for this patient. four-chamber and two-chamber views of echocardiograms acquired at end-diastole and end-systole are shown in Figure 3.18. Using single-plane (sp) and biplane (bp) Simpson's method, LV volumes at end-diastole and end-systole with Bi-V ICD on were estimated and compared with those reported from cardiac echo reports (Table 3.5). Since echocardiograms were not obtained with Bi-V ICD off, LV volumes could not be obtained. However, with an assumption that bi-ventricular pacing does not have an acute effect on the loading conditions of the LV (i.e. the end-diastolic LV volume), they were estimated using the relation:

$$CO = SV \times HR \qquad \text{(Eqn 3.1)}$$

where CO = Cardiac output
SV = Stroke volume = EDV-ESV
HR = Heart rate

Cardiac outputs for biventricular pacing (Bi-V ICD on) and atrial pacing (Bi-V ICD off) measured with Doppler echocardiography were The patient's heart was paced at 70 bpm during both biventricular (Bi-V ICD on) and atrial (Bi-V ICD off) pacing and cardiac outputs were 3.67 and 2.70 L/min, respectively.

ECG and LV pressures recorded using Clearsign$^{TM}$ Bard electrophysiologic recorder system with Bi-V ICD turned on are shown in Figure 3.19. Measurements were made with Bi-V ICD turn off as well. Using ECG

recordings that provide information about the stages of the cardiac cycle to which these volumes and pressures correspond, the LV pressure-volume loop can be constructed for different cardiac cycles.

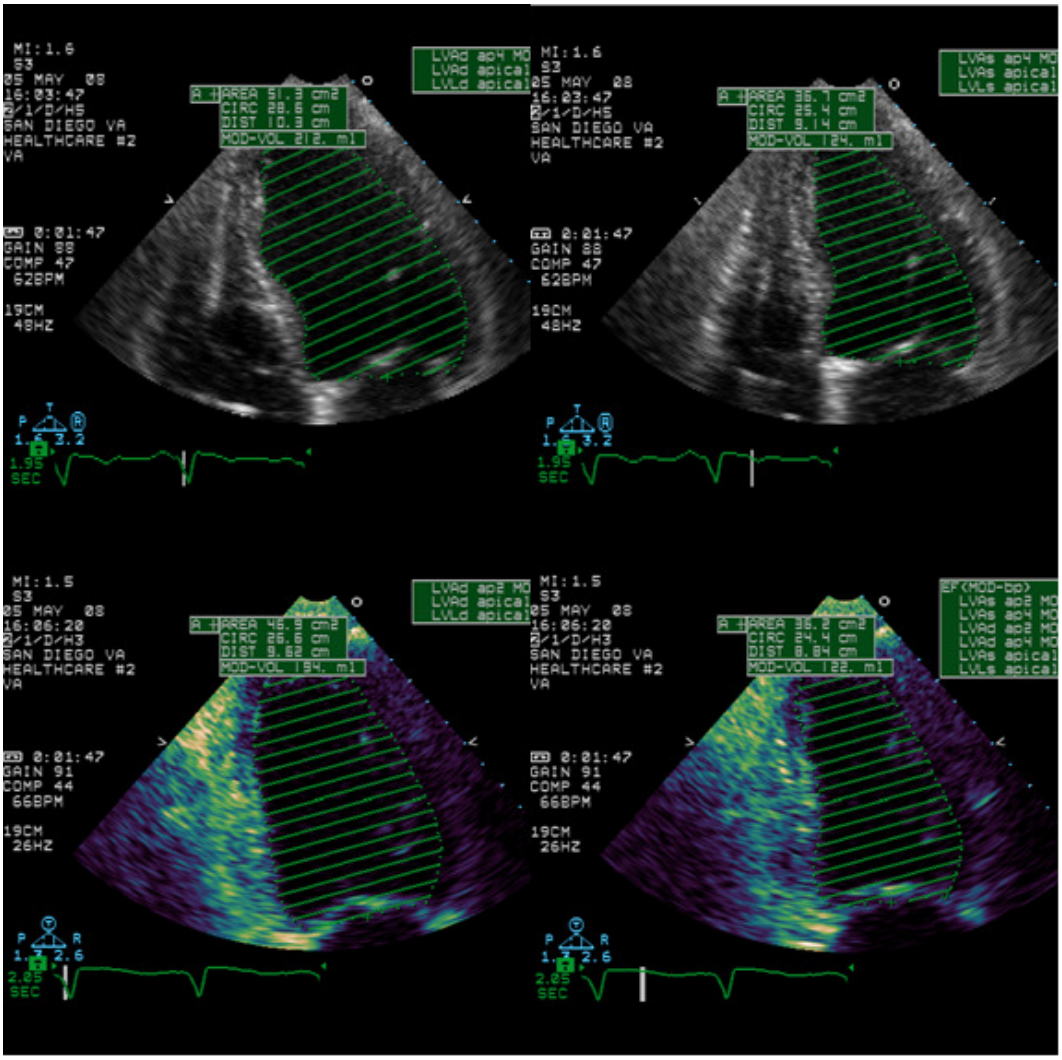


**Figure 3.18:** Four-chamber (Top row) and two-chamber (Bottom row) views of 2D transthoracic echocardiograms obtained at end-diastole (left column) and end-systole (right column) with Bi-V turned on.

**Table 3.5:** Comparison between LV volumes from cardiac echo reports and those calculated using Simpson's method (ED: end-diastole, ES: end-systole, EF: ejection fraction, sp2: single-plane 2-chamber view, sp4: single-plane 4-chamber view, bp: biplane)

| | | Bi-V ICD on | | | Bi-V ICD off (calculated) | | |
|---|---|---|---|---|---|---|---|
| | | ED | ES | EF | ED | ES | EF |
| Reported LV Vol (mL) | sp2 | 194.0 | 122.0 | 0.371 | 194.0 | 153.3 | 0.210 |
| | sp4 | 212.0 | 124.0 | 0.419 | 212.0 | 171.3 | 0.192 |
| | bp | 213.0 | 127.0 | 0.404 | 213.0 | 172.3 | 0.191 |
| Calculated LV Vol (mL) | sp2 | 189.7 | 128.6 | 0.322 | 189.7 | 149.0 | 0.215 |
| | sp4 | 217.4 | 118.14 | 0.457 | 217.4 | 176.7 | 0.187 |
| | bp | 209.6 | 125.2 | 0.403 | 209.6 | 168.9 | 0.194 |

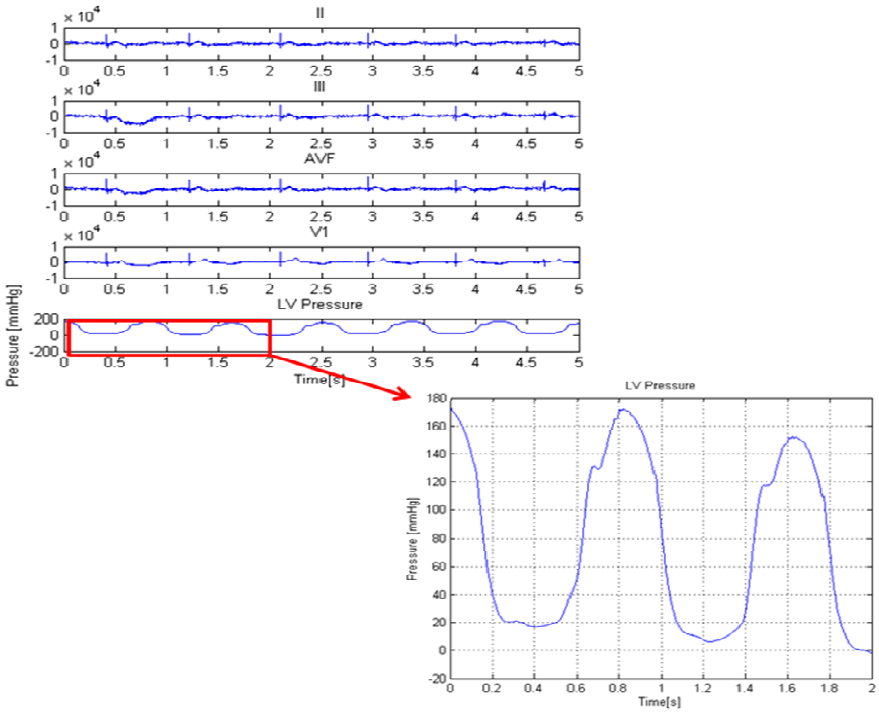


**Figure 3.19:** ECG and LV pressures measured using Clearsign™ Bard electrophysiologic recorder system with Bi-V ICD turned off.

# Chapter 4

# Discussion

Computational models have great potential to predict the complex electromechanical behavior of the heart in normal and diseased states. Due to individual variability in structure, electrical and mechanical properties, and response to pathophysiological conditions, it is important to include patient-specific parameters in computational models in order to faithfully reproduce the electromechanical behavior of an individual's heart. Once a complete patient-specific computational model is built, it is possible to explore its capabilities to predict the behavior of the heart in response to certain conditions, such as myocardial infarction and LBBB. To facilitate the idea of using patient-specific

computational models to increase the efficacy of CRT in patients with CHF, it is important to design efficient, accurate methods to generate models from various clinical measurements. In this thesis, methods for development of three-dimensional patient-specific computational models of ventricular electromechanics in the failing human heart were presented. Specifically, patient-specific geometric model development based on image segmentation and two-dimensional anatomic mesh fitting were described. In addition, methods for modeling the fiber architecture based on DTMRI data and modeling the activation pattern using electroanatomic endocardial activation time measurements were discussed in detail. Lastly, a method for estimating dynamic LV volumes, which are useful for estimating patient-specific mechanical and circulatory parameters, was presented. The results of the proposed methods and their significance on development of patient-specific computational models to predict and optimize the outcomes of CRT, and to gain better understanding of electromechanics of the heart in normal and diseased conditions, are discussed in the following sections. Furthermore, various problems associated with certain aspects of clinical measurements and ways, if any, to overcome these issues are discussed.

## *4.1 Cardiac CT and Image Segmentation*

Cardiac CT images are important measurements as they provide the most accurate and detailed information about ventricular structure. Despite its importance, the CT images of the patient's heart were obtained in a sub-optimal fashion and contained several types of artifacts that made segmentation

extremely difficult. The misregistration artifacts that appeared as sudden jumps in the CT data (Figure 4.1A) were the major issues. Such artifacts may occur in patients with arrhythmia due to irregular heart rhythm. Although it would be ideal to avoid them as much as possible for better and easier segmentation, ECG editing techniques could potentially be used to correct such type of artifacts. In addition, the CT scanning window was not properly positioned at the time of data acquisition and thus, some parts of the heart were not scanned (Figure 4.1B).

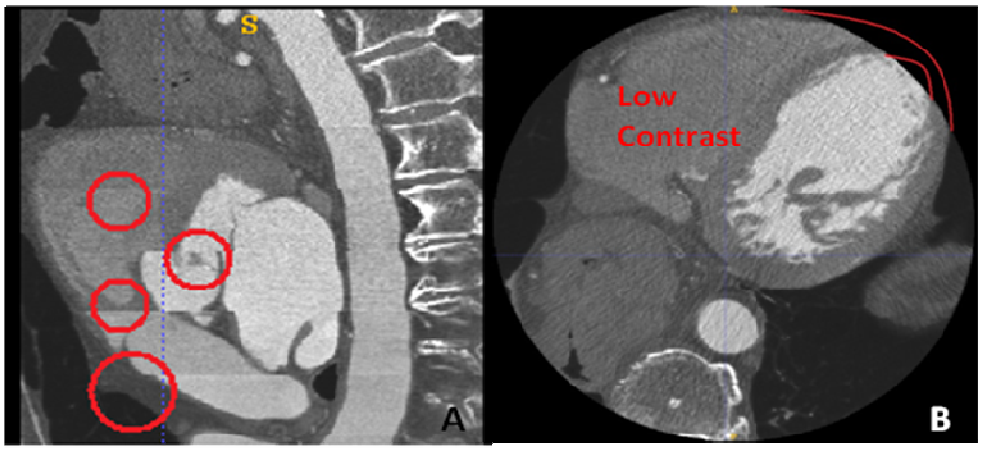


**Figure 4.1:** CT images showing artifacts due to A) misregistration (red circles) B) improper positioning of scanning window and low contrast in right ventricle.

Lastly, the contrast between the right ventricle and the myocardial tissue was very low (Figure 4.1B) and thus, active contour methods could not be performed successfully.

In the absence of the artifacts in the CT data, the semi-automatic segmentation using active contour methods can be performed rather than the manual delineation of endocardial and epicardial surfaces. Shown in Figure 4.2 is an example of semi-automatic segmentation results for MRI data of a dog heart

produced in our group [56]. The semi-automatic segmentation allows for much more robust and accurate segmentation by eliminating the need for manual handling of the data which can easily introduce errors. For future studies with more HF patients, cardiac CT protocols need to be adjusted and carefully reviewed to avoid such artifacts that may require tedious manual procedures and estimations which may introduce greater errors.

It is noteworthy that the ventricular geometry was imaged at end-diastole and was already experiencing a significant amount of load. If not taken into account, this may lead to incorrect numerical calculations and the mechanical behavior of the failing heart cannot be faithfully reproduced. In future studies, efficient methods for predicting the unloaded configuration of the three-dimensional finite element model generated based on the CT images acquired at end-diastole must be developed. An algorithm developed by S. de Putter *et al* [57], in which a backward incremental method was used to predict the unloaded geometry of abdominal aortic aneurysms with the loaded geometry and applied load as initial conditions, demonstrates highly promising results and may be adapted to this specific application.

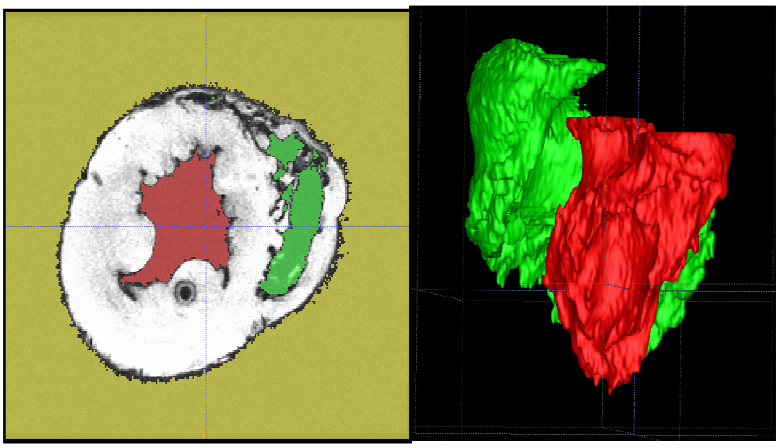

**Figure 4.2:** Results of a semi-automatic segmentation using active contour methods. **(left)** Axial slice with the three segmentation labels colored in red for LV, green for RV, and yellow for outside free-space. **(right)** 3D rendering of the RV and LV segmentation labels.

## *4.2 DTMRI and Fiber Architecture*

DTMRI has recently been recognized as an important imaging technique which allows for measurement of cardiac fiber orientations. In this thesis, a method to model the fiber architecture of a human heart using DTMRI was developed and tested on a simple cubic mesh with synthetic data which consisted of 6 independent diffusion coefficients. As shown in Figure 3.11, the eigenvectors computed from eigenvalue decomposition of the diffusion tensor resulted in fiber angles that closely matched the fiber angles from the original synthetic data. The result suggests that the proposed method, if two or more elements in the transmural direction are used along with sufficient number of data points within each element, can achieve fiber angles that are sufficiently

close to those in the original data set. Therefore, more elements across the ventricular walls will lead to substantially more accurate results at least when trilinear basis functions are used in fitting the diffusion coefficients. The significance of the proposed method is that it can be used to accurately model the cardiac fiber architecture based on the information extracted from DTMRI data which can be acquired in a day for full measurements for a single heart. Using the proposed method and DTMRI technique, the entire process of modeling cardiac fiber architecture can be performed in a few days as compared to the histological approach, which typically takes several months for low-resolution fiber angle measurements for a single heart.

## *4.3 Endocardial Activation Maps*

The activation times throughout the whole myocardium are one of the most important patient-specific model parameters that have a significant influence on the electrophysiology of the heart. To estimate the activation patterns throughout the whole myocardium, the endocardial activation maps are needed so that external stimuli may be applied to the earliest activated regions from these endocardial activation maps and monodomain conductivities can be adjusted to obtain activation patterns across the ventricular walls.

To generate endocardial activation maps, electroanatomic mapping techniques were utilized to measure activation timings on the endocardial surfaces of the ventricles. The activation maps were generated for both ventricles by fitting electroanatomic endocardial activation time measurements on the

endocardial surfaces. The resulting LV endocardial activation map was in a good agreement with the electroanatomic endocardial activation time measurements, with an RMS fitting error of 0.9271 ms. The data points were fairly well-distributed throughout the LV endocardial surface. The RV endocardial activation map successfully captured the general activation patterns from the measurements, but exhibited a slightly poorer agreement with them (RMS fitting error =1.1476 ms). This is mainly due to the fact that distribution of the RV data points was not quite even; there were elements on the RV endocardium in which a large number of measurements were concentrated while other elements had only a smaller number of or even no data points. This is an inherent limitation of electroanatomic mapping techniques as the catheters cannot reach everywhere within the ventricles for activation time measurements. The measurement locations heavily depend on the patient-specific geometry of the ventricles as well as the physician's skills.

The undesirable effects of such uneven distribution of data points for the ventricles were overcome to a certain extent by using smoothing weights that improved the smoothness of the activation time map generated by fitting the activation time measurements on the endocardial surfaces of the ventricles in the 2D surface model. Using $\alpha = 0.1$ as the smoothing weight corrected for major artifacts caused by the lack of data points in certain regions and yielded a significant improvement in smoothness of the activation maps with only a slight compensation in the RMS fitting error. The results suggest that activation of the RV endocardial surface occurs significantly earlier than that of the LV

endocardial surface. This is expected since the HF patient had an LBBB, in which the conduction of electrical impulses to the left ventricle is slowed, resulting in a delayed activation and contraction of the left ventricle.

## *4.4 LV Volume Estimation*

In patient-specific model development, accurate estimation of dynamic LV volumes is useful in many ways. First of all, passive and active mechanical parameters of the cardiac tissue can be estimated from EDPVR and ESPVR that are determined from end-diastolic and end-systolic LV pressure and volume measurements obtained from multiple cardiac cycles. Certain circulatory parameters can also be estimated from these measurements. Furthermore, the P-V loop constructed from the dynamic LV pressure and volume measurements is a good means to evaluate the global LV function and to validate the model. Lastly, the stroke work, which is defined as the area within the P-V loop may be useful for fine tuning of the model in later stages of model development. Therefore, a reliable method to estimate the LV cavity volumes at any time point during a cardiac cycle would be highly valuable. In this thesis, Simpson's method was proposed to achieve this goal and was tested at end-diastole and end-systole. LV volumes were estimated assuming circular cross-sectional areas for single-plane echocardiograms of two-chamber and four-chamber views, and assuming elliptical cross-sectional areas using the information from these two views. LV volumes calculated using Simpson's method were comparable to the

reported values, demonstrating that it can be used to accurately estimate LV cavity volumes at any time point during a cardiac cycle.

Simpson's method for LV volume estimation requires accurate determination of the LV endocardial border as well as the long axis of the LV. The determination of LV endocardial border is done manually by the operator as automated LV edge-detections algorithms do not give accurate results due to the low quality of echocardiograms. This may result in a significant variability in LV volumes estimated by different operators. Therefore, high-quality echocardiograms with well-defined endocardial borders are important in the successful estimation of LV volumes. In addition, although Simpson's method works well for both single-plane and biplane echocardiograms in estimating LV volumes, the results from biplane echocardiograms are generally more reliable as an elliptical disc better approximates the cross-sectional area at each level along the long axis of the heart.

It is worthwhile to note that construction of EDPVR and ESPVR was not possible for the particular CHF patient involved in this study as echocardiograms were obtained for a period of less than 2 cardiac cycles. To determine EDPVR and ESPVR accurately, end-diastolic and end-systolic LV pressure and volume measurements from multiple cardiac cycles are needed. Moreover, the pressure measurements and echocardiograms were not acquired concurrently and therefore, the resulting P-V loops may not accurately describe the global left ventricular function.

# Chapter 5

# Conclusions

Patient-specific computational models offer a large potential for studying the complex electromechanical behavior of the heart in its normal and diseased states and for clinical applications such as improving the efficacy of CRT in patients with an intraventricular conduction delay. For this reason, significant efforts have been made in our group to develop protocols for building specific models in the dogs and demonstrate the predictive capabilities of these models by comparison with experimental results. The next logical step would be to explore the clinical feasibility of these computational models as well as the degree of benefits they can offer to physicians in planning surgical procedures

that will achieve optimal clinical outcomes. Therefore, a central focus of this study was to develop methods for building patient-specific computational models in patients with dyssynchronous heart failure from various clinical measurements. This work highlighted the development of methods for four different components that are essential in building patient-specific computational models: 3D ventricular geometry, cardiac fiber architecture, endocardial activation maps, and LV volume estimation from echocardiograms for mechanical and circulatory parameter estimation.

The proposed method for modeling the 3D ventricular geometry allowed for generation of an accurate 3D geometric model of the failing human heart based on cardiac CT data. Since ventricular geometry is one the major model parameters that determines the cardiac function, establishing an efficient method for accurately modeling the 3D ventricular geometry is a crucial step for building patient-specific models.

The method developed for modeling cardiac fiber architecture is capable of incorporating fiber orientations from DTMRI in the 3D geometric model. Histological procedures for fiber angle measurements, which may take several weeks or even months for a complete measurement of a single heart, can be avoided with this method by extracting information about cardiac fiber architecture directly from DTMRI data which can be obtained in a single day.

The 3D activation sequence is another major model parameter. According to a sensitivity analysis performed in our lab, the influence of the activation sequence and the 3D ventricular geometry on cardiac function is at least several

times more significant than other model parameters. Endocardial activation maps are an important starting point in estimating the 3D activation sequence across the ventricular walls. Therefore, the method developed for generating endocardial activation maps of LV and RV based on electroanatomic activation time measurements will be an important tool for obtaining realistic 3D activation sequences.

Lastly, accurate estimation of LV volumes throughout cardiac cycle is important for determining the active and passive mechanical parameters of the cardiac tissue. The technique described in this thesis demonstrated its potential for this application by obtaining good estimates LV volumes from single-plane and biplane echocardiograms. However, the proposed method is prone to errors resulting from operator-dependent manual procedures and limitations of current ultrasound imaging system that lead to unclear endocardial borders. An alternative approach to obtain LV volumes would be to passively inflate the 3D patient-specific FE model by applying a known magnitude of pressure and calculate the resulting volume of the cavity. Since the 3D FE model was built from cardiac CT data which provide more reliable, detailed information about the patient-specific ventricular geometry, a higher accuracy is expected in estimating LV volumes.

The methods developed in this thesis serve to facilitate development of patient-specific cardiac models with high accuracy and efficiency. Although many animal models have been developed in the past, very few attempts have been made to build a 3D computational model of the human heart. We believe that this

study is, to the best of our knowledge, one of the very first attempts to build a patient-specific computational model of the failing human heart with LBBB by integrating information from multiple clinical measurements, and to ultimately demonstrate its potential to aid physicians in surgical planning to achieve optimal therapeutic outcomes. Although computational models built in such a way may not be able to make absolute predictions of the therapeutic outcomes as the reference system cannot be defined from the clinical measurements discussed in this thesis, we believe that they will be invaluable tools that will help gain better understanding of cardiac electromechanics and improve efficacy of cardiac resynchronization therapy.

## Acknowledgments

This work was supported by NIH, Medtronic, Inc., and UCSD Von Liebig Center for Entrepreneurship and Technology Advancement. The DTMRI data for normal human heart was provided by Drs. Patrick Helm and Raimond L. Winslow at the Center for Cardiovascular Bioinformatics and Modeling and Dr. Elliot McVeigh at the National Institute of Health. The data may be accessed on the internet at www.ccbm.jhu.edu.

# References


1. Katz AM. *Physiology of the heart.* Philadelphia, PA: Lippincott Williams & Wilkins, 2001.

2. Streeter DD Jr. Gross morphology and fiber geometry of the heart. Handbook of Physiology, Section 2: The Cardiovascular System, Chapter 4, M BR. Bethesda, MD, American Physiological Society: I:61, 1979.

3. LeGrice IJ, Smaill BH, Chai LZ, Edgar SG, Gavin JB, and Hunter PJ. Laminar structure of the heart: ventricular myocyte arrangement and connective tissue architecture in the dog. *Am J Physiol Heart Circ Physiol* 266:H571-H582*,* 1995*.*

4. Arts T, Costa KD, Covell JW, and McCulloch AD. Relating myocardial laminar architecture to shear strain and muscle fiber orientation. *Am J Physiol Heart Circ Physiol* 280: H2222–H2229, 2001.

5. Ennis DB. Assessment of myocardial structure and function using magnetic resonance imaging. PhD thesis, Johns Hopkins University, Baltimore, Maryland, 2004.

6. Mall FP. On the muscular architecture of the ventricles of the human heart. *Am. J. Anat.* 11:211–266, 1911.

7. Streeter DD Jr, Vaishnav RN, Patel DJ, Spotnitz HM, Ross J, Sonnenblick EH. Stress distribution in the canine left ventricle during diastole and systole. Biophys Y 10: 345-363, 1970.

8. Streeter DD Jr and Hanna WT. Engineering mechanics for successive states in canine left ventricular myocardium. ii. fiber angle and sarcomere length. *Circ. Res*, 33:656–664, 1973.

9. Ross AA and Streeter DD Jr. Myocardial fiber disarray. *Circulation*, 60:1425–1426, 1979.

10. Takayama Y, Costa KD, and Covell JW. Contribution of laminar myofiber architecture to load-dependent changes in mechanics of LV myocardium. *Am J Physiol Heart Circ Physiol* 282: H1510-H1520, 2002.

11. Scollan DF, Holmes A, Zhang J, and Winslow RL. Reconstruction of Cardiac Ventricular Geometry and Fiber Orientation Using Magnetic Resonance Imaging. *Ann Biomed Eng* 28: 934-944, 2000.

12. Ashikaga H, Omens JH, and Covell JW. Time-dependent remodeling of transmural architecture underlying abnormal ventricular geometry in chronic volume overload heart failure. *Am J Physiol Heart Circ Physiol* 287: H1994-H2002, 2004.

13. Ashikaga H, Omens JH, Ingels NB, Jr., and Covell JW. Transmural mechanics at left ventricular epicardial pacing site. *Am J Physiol Heart Circ Physiol* 286: H2401-H2407, 2004.

14. Costa KD, Takayama Y, McCulloch AD, and Covell JW. Laminar fiber architecture and three-dimensional systolic mechanics in canine ventricular myocardium. *Am J Physiol* 276: H595-H607, 1999.

15. Streeter DD Jr, Spotnitz HM, Patel DP, Ross J Jr, and Sonnenblick EH. Fiber orientation in the canine left ventricle during diastole and systole. *Circ Res* 24: 339-347, 1969.

16. Helm PA, Younes L, Beg MF, Ennis DB, Leclercq C, Faris OP, McVeigh ER, Kass DA, Miller MI, Winslow RL. Evidence of structural remodeling in the dyssynchronous failing heart. *Circulation Res* 98: 125-132, 2006

17. Levy MN, Pappano AJ. *Cardiovascular physiology*.Elsvier Health Sciences, Philadelphia. 2006.

18. McCulloch AD, Hunter PJ, and Glass L. Theory of Heart. Biomechanics, Biophysics, and Nonlinear Dynamics of Cardiac Function. New-York City: *Springer-Verlag*, 1989.

19. Guccione JM, Waldman LK, and McCulloch AD. Mechanics of active contraction in cardiac muscle: Part II--Cylindrical models of the systolic left ventricle. *J Biomech Eng* 115: 82-90, 1993.

20. Y.C. Fung. *Biomechanics: Mechanical Properties of Living Tissues.* Spinger-Verlag, New York, 1981.

21. Okamoto RJ, Moulton MJ, Peterson SJ, Li D, Pasque MK, and Guccione JM. Epicardial suction: A new approach to mechanical testing of the passive ventricular wall. *J Biomech Eng-Transactions of the ASME* 122: 479-487, 2000.

22. Omens JH, MacKenna DA, and McCulloch AD. Measurement of strain and analysis of stress in resting rat left ventricular myocardium. *J Biomech* 26: 665-676, 1993.

23. Vetter FJ and McCulloch AD. Three-Dimensional Stress and Strain in Passive Rabbit Left Ventricle: A Model Study. *Ann Biomed Eng* 28: 781-792, 2000.

24. Guccione JM and McCulloch AD. Mechanics of active contraction in cardiac muscle: Part I--Constitutive relations for fiber stress that describe deactivation. *J Biomech Eng* 115: 72-81, 1993.

25. Lloyd-Jones DM, Larson MG, Leip EP, Beiser A, D'Agostino RB, Kannel WB, Murabito JM, Vasan RS, Benjamin EJ, and Levy D. Lifetime Risk for Developing Congestive Heart Failure: The Framingham Heart Study, 3068-3072, 2002.

26. Zheng ZJ, Croft JB, Giles WH, and Mensah GA. Sudden cardiac death in the United States, 1989 to 1998. Circulation 104: 2158-2163, 2001.

27. Rosamond W, Flegal K, Furie K, Go A, Greenlund K, Haase N, Hailpern SM, Ho M, Howard V, Kissela B, Kittner S, Lloyd-Jones D, McDermott M, Meigs J, Moy C, Nichol G, O'Donnell C, Roger V, Sorlie P, Steinberger J, Thom T, Wilson M, Hong Y, and for the American Heart Association Statistics Committee and Stroke Statistics S. Heart Disease and Stroke Statistics--2008 Update: A Report From the American Heart Association Statistics Committee and Stroke Statistics Subcommittee, e25-146, 2008.

28. McMurray JJ, Pfeffer MA. Heart failure. *Lancet* 365:1877–89, 2005.

29. The CONSENSUS Trial Study Group. Effects of enalarpril on mortality in severe congestive heart failure. Results of the Cooperative North Scandinavian Enalapril Survival Study (CONSENSUS). N Engl J Med 316:1429-1435, 1987.

30. The SOLVD Investigators. Effect of enalapril on survival in patients with reduced left ventricular ejection fractions and congestive heart failure. N Engl J Med 325:293–302, 1991.

31. The Digitalis Investigation Group. The effect of digoxin on mortality and morbidity in patients with heart failure. N Engl J Med 336:525–533, 1997.

32. Pitt B, Zannad F, Remme WJ, Cody R, Castaigne A, Perez A, et al. The effect of spironolactone on morbidity and mortality in patients with severe heart failure. Randomized Aldactone Evaluation Study Investigators. N Engl J Me; 341:709–717, 1999.

33. Buxton AE, Lee KL, Fisher JD, et al. A randomized study of the prevention of sudden death in patients with coronary artery disease. Multicenter Unsustained Tachycardia Trial Investigators. N Engl J Med 341:1882–1890, 1999.

34. Moss AJ, Zareba W, Hall WJ, et al. Prophylactic implantation of a defibrillator in patients with myocardial infarction and reduced ejection fraction. N Engl J Med 346:877–883, 2002.

35. Rose EA, Gelijns AC, Moskowitz AJ, et al. Long-term mechanical left ventricular assistance for end-stage heart failure. N Engl J Med 345:1435–1443, 2001.

36. Bleumink GS, Knetsch AM, Sturkenboom MCJM, Straus SMJM, Hofman A, Deckers JW, Witteman JCM, and Stricker BHC. Quantifying the heart failure epidemic: prevalence, incidence rate, lifetime risk and prognosis of heart failure: The Rotterdam Study 1614-1619, 2004.

*37.* Xiao HB, Roy C, Fujimoto S, and Gibson DG. Natural history of abnormal conduction and its relation to prognosis in patients with dilated cardiomyopahty. *International Journal of Cardiology* 53: 163-170, 1996.

38. Usyk TP, McCulloch AD. Computational Methods for Soft Tissue Biomechanics. In Holzapfel GA, Ogden RW (Eds) *Biomechanics of Soft Tissue in Cardiovascular Systems.* Springer, Wien New York (CISM Courses and Lectures No. 441, International Center for Mechanical Sciences), pages 273-342, 2003.

39. Belik ME, Usyk TP, McCulloch AD. Computational Methods for Cardiac Electrophysiology. In Ayache N, (Guest Ed) *Computational Models for the Human Body,* Special Volume of (Ciarlet PG, Ed) *Handbook of Numerical Analysis,* Volume XII. Elsevier B.V., pages 129-188, 2004

40. Kerckhoffs RCP, Faris OP, Bovendeerd PHM, Prinzen FW, Smits K, McVeigh ER, and Arts T. Electromechanics of paced left ventricle simulated by straightforward mathematical model: comparison with experiments, Am J Physiol Heart Circ Physiol 289:H1889-1897, 2005.

41. Usyk TP, LeGrice IJ, and McCulloch AD. Computational model of three-dimensional cardiac electromechanics. *Computing and Visualization in Science* 4: 249-257, 2002.

42. McCulloch, AD. “Multi-Scale Modeling Environment for Tissue and Organ Biophysics.” Department of Bioengineering, University of California, San Diego, 30 Oct. 2008.

43. Baker, et al. Acute Evaluation of programmer-guided AV/PV and VV Delay optimization comparing an IEGM method and echocardiogram for cardiac resynchronization therapy in heart failure patients and dual-chamber ICD implants. *J Cardiovasc Electrophysiol*. 18:185-191, 2007.

44. Quinones MA, Otto CM, Stoddard M, Waggoner A, Zoghbi WA. Recommendations for quantification of Doppler echocardiography: a report from the Doppler Quantification Task Force of the Nomenclature and Standards Committee of the American Society of Echocardiography. *J Am Soc Echocardiogr* 15:167-84, 2002.

45. J. W. Demmel, *Applied Numerical Linear Algebra*, SIAM, Philadelphia, 1997.

46. G. H. Golub and C. F. Van Loan, *Matrix Computation*, 3rd ed., Academic Press, Boston, 1996.

47. G. Strang, *Introduction to Linear Algebra*, 2nd ed., Wellesley-Cambridge Press, Cambridge, MA, 1998.

48. Muller, N., Magaia, L. and Herbst B.M. Singular value decomposition, eigenfaces, and 3D reconstructions. *SIAM Review* 46: 518–545, 2004.

49. Streeter DD, Jr and Hanna WT. Engineering mechanics for successive states in canine left ventricular myocardium. I. Cavity and wall geometry. *Circ. Res.* 33:639–655, 1973.

50. Mazhari R, Omens JH, Waldman LK, McCulloch AD. Regional myocardial perfusion mechanics: a model-based method of analysis. *Ann Biomed Eng* 26:743-755, 1998.

51. Zhukov L, Barr AH. Heart-muscle fiber reconstruction from diffusion tensor MRI. Proceedings of the 14th IEEE Visualization 2003. October 19–24: 597– 602, 2003.

52. Tseng WY, Reese TG, Weisskoff RM, and Wedeen VJ. Cardiac diffusion tensor MRI in vivo without strain correction. *Magn Reson Med* 42: 393–403, 1999.

53. Hsu E, and Henriquez, C. Myocardial fiber orientation mapping using reduced encoding diffusion tensor imaging. *J Cardiovasc Magn Reson* 3: 339–347, 2001.

54. Sachse FB, Henriquez C, Seemann G, Riedel C, Werner CD, Penland R C, Davis B, and Hsu E. Modeling of fiber orientation in the ventricular myocardium with MR diffusion imaging. In *Proc. Computers in Cardiology* 28:617–620, 2001.

55. Helm PA, Beg MF, Miller MI., Winslow RL. Measuring and Mapping Cardiac Fiber and Laminar Architecture Using Diffusion Tensor MR Imaging. *Annals NY Acad Sci* 1047:296-307, 2005.

56. Chang A, Towbin J. *Heart Failure in Children and Young Adults*. Saunders Elsevier, Philadelphia. 2005

57. Forster V. Design of a multi-scale canine-specific model of cardiac electromechanics: A step toward patient specific modeling. Master's thesis, p.20, 2008.

58. de Putter S, Wolters BJBM, Rutten MCM, Breeuwer M, Gerritsen FA, van de Vosse FN. Patient-specific initial wall stress in abdominal aortic aneurysms with a backward incremental method. *J Biomech* 40:1081–1090, 2007.